Modification of fumarolic gases by the ice-covered edifice of Erebus volcano, Antarctica

T. Ilanko[1], T.P. Fischer[2], P. Kyle[3], A. Curtis[4], H. Lee[5], Y. Sano[6]

1. Department of Geography, University of Sheffield, Sheffield S10 2TN, UK

2. Department of Earth & Planetary Sciences, University of New Mexico, NM 87131, USA

3. Department of Earth & Environmental Science, N.M. Institute of Mining and Technology, Socorro, NM 87801, USA

4. Jet Propulsion Laboratory, Pasadena, CA91109, USA

5. School of Earth and Environmental Sciences, Seoul National University, 1 Gwanak-ro, Gwanak-gu, 08826 Seoul, South Korea

6. Institute of Atmosphere and Ocean Research, The University of Tokyo, Chiba, Japan

Abstract

The chemistry of gases measured in ice caves and from warm geothermal ground at Erebus volcano, Antarctica, show that gas emissions are dominated by air, with varying amounts of added volcanic CO_2. This suggests widespread circulation of air through the volcanic edifice, as well as spatially or temporally varying contributions from magmatic degassing.

The resulting gases are further modified by two processes. The first is CO_2 dissolution in water, resulting in fractionation from magmatic $\delta^{13}C$-CO_2 values, which are estimated to be around -4‰, to heavier values, up to -1‰. Assuming all magmatic CO_2 is dissolved in neutral water as HCO_3^-, this requires hydrothermal temperatures of over 120°C. However, other phases such as calcite may be present, likely implying even higher temperatures, while lower water pH values could result in similar isotope ratios at much lower temperatures, such as 60°C at pH of 5.3. A large proportion of magmatic CO_2 must be lost to this hydrothermal system or to mixing with air. The hydrothermal influence is localized to certain areas on the volcano, which may be associated with high velocity zones identified in previous studies by seismic tomography. Two sites with stronger magmatic signatures, by contrast, are above low velocity zones representing possible shallow magma storage.

The second modification is the removal of oxygen from both deeply-sourced and air-derived gases. This is likely due to prevailing conditions in the subsurface, as it is independent of the original source of the gases and of hydrothermal modifications, and thus may affect sites with magmatic, air-like, or hydrothermal signatures.

34

1. Introduction

1.1   Hydrothermal systems at snow- or ice-covered volcanoes.

Near surface heat and fumarolic gas emission on glaciated and snow-covered volcanoes, cause melting and sublimation of the ice and snow and can result in the formation of fumarolic ice caves (FIC) (Curtis and Kyle, 2011, 2017). Globally, FIC have been described on only a few volcanoes, including Erebus and Mount Melbourne in Antarctica (Lyon and Giggenbach, 1974), and Mount Rainier (Zimbelman et al., 2000), Mount Baker, and Mount St Helens in the Cascades. However, it has been suggested that such systems may be more common and widely distributed than the few known examples (Curtis and Kyle, 2017).

FIC conveniently reveal fumarolic or diffuse degassing sites that might be hard to observe on a volcano without ice or snow cover. Understanding this degassing and potential hydrothermal circulation at glaciated volcanoes also has implications for volcanic hazards. These include the likelihood of phreatic or phreatomagmatic eruptions, or reduced slope stability due to hydrothermal alteration. Monitoring gas emissions or ice cover at active volcanoes could be important in identifying changes to heat flow and degassing that result from changes in shallow magmatic or hydrothermal systems. Moreover, glaciation and deglaciation may act on a large scale as controls on volcanic activity and the climate, with the implication that decreasing ice cover can cause increases in carbon dioxide emissions, and thus warming (Huybers and Langmuir, 2009). Understanding degassing from glaciated volcanoes is important to both understanding past changes in climate and the implications of widespread ice loss in volcanic regions due to a warming climate. For example, over a hundred potential subglacial volcanoes have been identified in West Antarctica (van Wyk de Vries et al., 2018) as well as evidence for recent eruptions (Iverson et al., 2017), and possible ongoing magma movement (Lough et al., 2013).

Due to the more limited ice cover in its summit area and the accessibility of Erebus, it is one of the few sites where degassing of a glaciated volcano can be quantified. Erebus is unique among volcanoes currently hosting ice caves in that it exhibits long-term persistent degassing through an open conduit, with many studies focused on the dynamics and gas chemistry of its lava lake. However, also of interest in understanding its gas flux, and more relevant to glaciated volcanoes lacking open summit vents, is the persistent flank degassing on which our study focuses. The following section briefly describes the setting and volcanic activity of Erebus.

### 1.2   Tectonic setting, Antarctic volcanism and Erebus volcano

Erebus volcano is one of four volcanic centres on Ross Island at the southern end of the Terror Rift, which has the youngest extension in the West Antarctic Rift System (WARS) (Hall et al., 2007; Henrys et al., 2007). Although Erebus is presently the most active volcano in the WARS, degassing occurs at others (Mt Berlin, Marie Byrd Land; Mts Rittmann and Melbourne, northern Victoria Land). The WARS covers the margin between the Transantarctic Mountains and the crustal blocks, derived from the breakup of Gondwana, that make up much of West Antarctica (Behrendt et al., 1991). Extension across the rift dates from the Cretaceous and the end of subduction along the Gondwana margin, but there remains uncertainty about whether the WARS is still active (Martin et al., 2014; Harry et al., 2018), and the relationship between its tectonism and volcanic activity.

78 Late Cenozoic volcanism in the WARS has been attributed to mantle plumes or extension of the lower
79 lithosphere causing decompression melting (Kyle et al., 1992; Behrendt, 1999; Rocchi et al., 2002). According
80 to Rilling et al. (2009), the timing of rifting episodes and volcanism in the Terror Rift indicates decompression
81 melting, though additional heat input or a modified mantle composition with a lower solidus are required to
82 allow partial melting and volcanism. This is consistent with Panter et al. (2018) who attribute the
83 geochemistry of lavas in the northwest Ross Sea to subcontinental lithospheric mantle (SCLM) with
84 metasomatic veins formed by carbonate-rich partial melt from the asthenosphere, itself containing material
85 subducted at the Gondwana margin. Ross Island, however, may be an exception. The HIMU-like
86 composition of Ross Island lavas, and the presence of a seismic low velocity zone down to 1200 km beneath
87 Ross Island support the argument of Phillips et al. (2018) for upwelling from the asthenospheric mantle as the
88 source of volcanism. A mantle plume (Kyle et al., 1992) could also account for the large volume magmatism,
89 the radial arrangement of volcanic centres, and ongoing volcanism. No carbon isotope data are available for
90 xenoliths on Ross Island but Correale et al. (2017) report carbon isotope ratios of -4.5‰ to -2.5‰, with -
91 3.5‰ for samples containing high CO_2, in SCLM xenoliths from Northern Victoria Land. However, this may
92 differ further south beneath Ross Island, given the evidence for an asthenospheric source and the suggestion
93 by Phillips et al. (2018) that the metasomatized SCLM beneath Ross Island has been removed by mantle
94 upwelling.
95
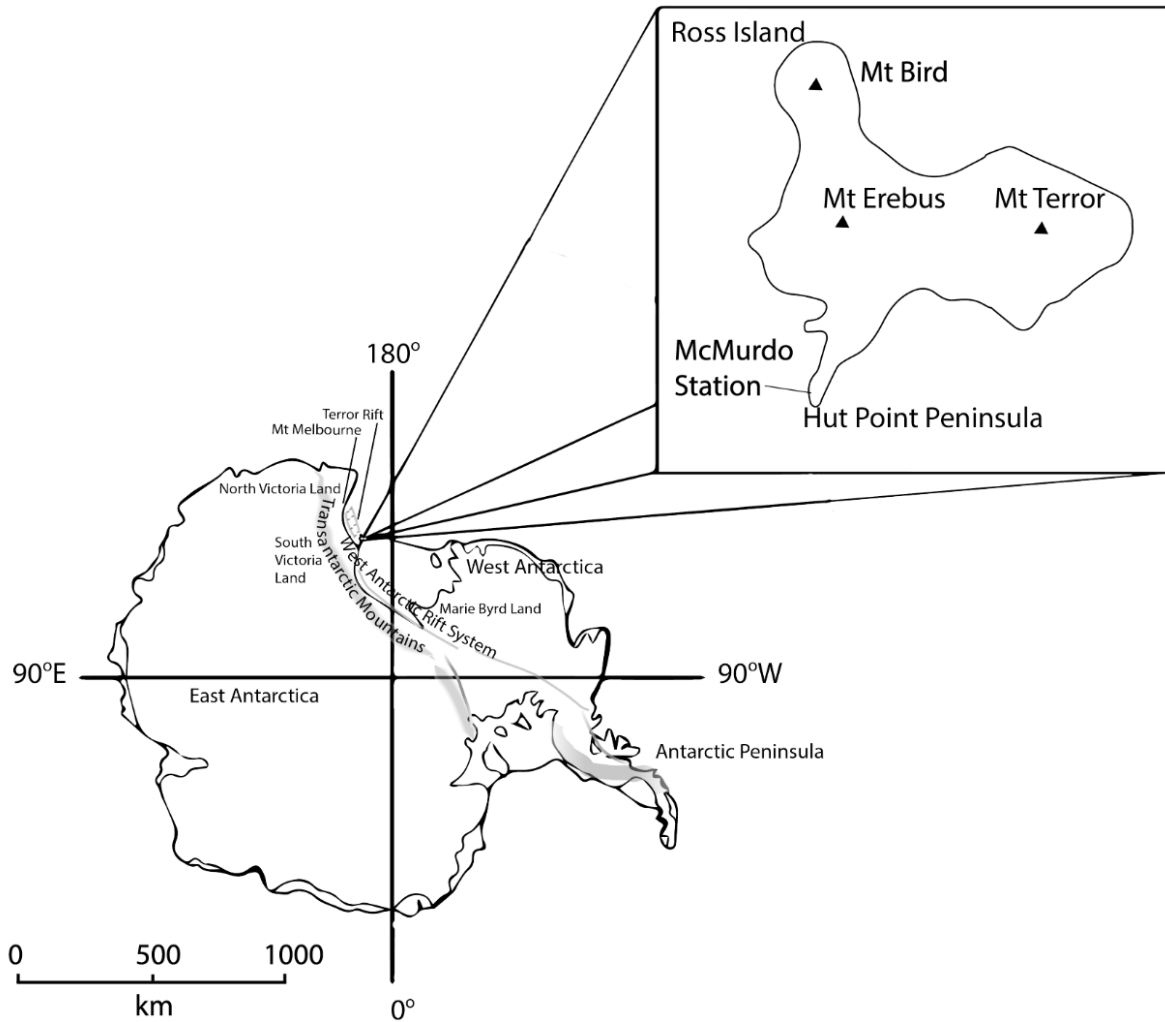
96
97   Figure 1. Location of Ross Island and Erebus. McMurdo Station and Scott Base are located on the southern
98   end of Hut Point Peninsula. WARS and Terror Rift after LeMasurier (1990, 2008).
99
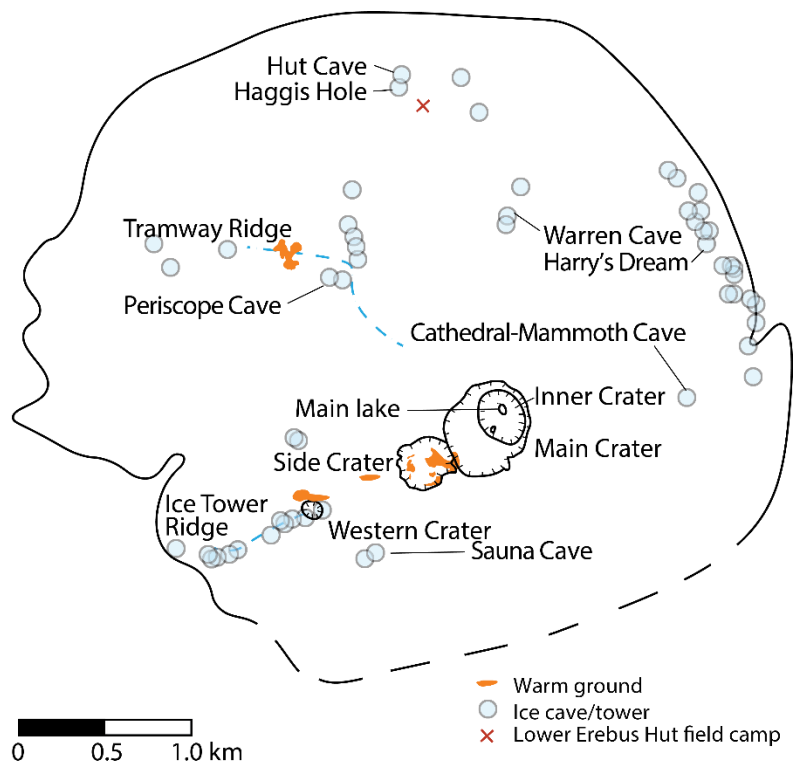
Figure 2. Erebus caldera, with craters, major ice towers, and ice caves. Warm ground areas include areas around Tramway Ridge (dashed line), Western Crater, and Side Crater. Data from Panter and Winter (2008), Curtis and Kyle (2010), and field observations.

Erebus is perhaps best known for the long-lived phonolite lava lake in its summit cone. This cone rises from a plateau on the upper flanks of the volcano, formed by two overlapping calderas at about 3400 m altitude, which contains over 100 FIC. Descriptions of many of these FIC, reported over several expeditions, are available through the Erebus caves database (Curtis and Kyle, 2010). At Erebus, the typical FIC is on the boundary between rock and snowpack, and not within a glacier, although it should be noted that ice density is closer to that of glacial ice than of firn (Curtis, 2015). A number of features of the caves are described by Curtis (2015) including barometric pumping at entrances, hot vents in the rock floors as well as cold vents on the surface through which outside air mixes in, and changes in the size and shape of caves between annual field seasons. Known areas of upper flank degassing on Erebus (Fig 1.) include Ice Tower Ridge (ITR), a line of small FIC extending from the southwest of the plateau through areas of warm ground on the flanks of the summit cone, and terminating at Side Crater, itself containing a number of fumaroles and warm ground areas (Panter and Winter, 2008). Other areas of interest include Tramway Ridge, which is an Antarctic Specially Protected Area (ASPA) of warm ground to the northwest of the summit cone, and more extensive caves located at various sites around the plateau including Hut Cave to the north, Warren Cave (NE), the sometimes-connected Cathedral-Mammoth system (SE), and Sauna (S).

The active magmatic system at Erebus degasses through the lava lake(s) and nearby high temperature vents with a composition rich in CO_2 relative to water and SO_2 (Oppenheimer and Kyle, 2008). Melt inclusions in Ross Island basanites, which are considered representative of the parental melt for the Erebus phonolite, contain up to 1.8% CO_2 (Rasmussen et al., 2017). Degassing at shallow depths is controlled by the solubility of the various volatile species, but CO_2, which is relatively insoluble, may be sourced from the mantle

126   (Oppenheimer et al., 2011). Based on plume gas chemistry and melt inclusion volatile contents, deep
127   degassing is likely to be the biggest contributor to the lava lake gas plume, followed by degassing from the
128   lava lake, with limited input from intermediate regions (Iacovino 2015). At shallow depths, seismic
129   tomography and interferometric studies by Zandomeneghi et al. (2013) identify several low- and high-velocity
130   zones within hundreds of metres below the surface of the Erebus summit plateau. They suggest that these
131   correspond to hot magma bodies or high permeability zones, and cooled intrusions or buried lava and caldera
132   rim features, respectively. The complex shallow magmatic plumbing has been attributed to possible restriction
133   of fluid flow by the latter. Both low- and high-velocity zones may influence the location of degassing features
134   such as ice caves, and the nature of subsurface structures may be reflected in the gas measured at the surface.
135
136   Ice and snow cover are variable around the Erebus caldera. Only limited meteoric water recharge is possible
137   in the arid climate, but localized melting of ice and snow, associated with heat from FIC and warm ground
138   areas, is evident. Groundwater on the Antarctic continent includes brines beneath the permafrost in the Dry
139   Valleys (Mikucki et al., 2015), and groundwater in ice-covered regions, where it may have some association
140   with subglacial volcanism (Christoffersen et al., 2014). The nature of a hydrothermal system on Erebus has
141   not been directly addressed before, although the presence of any substantial amount of liquid water within the
142   volcanic edifice will have implications in assessing potential hazards.
143
144   Volcanic activity on Erebus has mostly been stable over the past century or more, dominated by passive
145   degassing and small Strombolian explosions from the lava lake and adjacent vents. However, two significant
146   phreatic eruptions occurred in October 1993, emitting debris described by Dibble et al. (1994) as
147   hydrothermally altered. Evidence of phreatomagmatic activity in the Side Crater was found by Panter &
148   Winter (2008) and attributed to melting from the surface or permafrost, or to shallow hydrothermal water.
149   Distal tephra layers indicate that frequent phreatoplinian eruptions have occurred in the past (Harpel et al.,
150   2008; Iverson et al., 2014) but these have been explained as a result of snow or ice accumulation within the
151   crater.
152
153   Here, we report gas compositions, carbon isotope and nitrogen isotope data, and CO_2 fluxes, which reflect
154   sources of degassing and modification by crustal or hydrothermal processes. Wardell et al. (2003) previously
155   investigated CO_2 fluxes and carbon isotope ratios at ice towers and warm ground areas, suggesting that the
156   measured carbon isotope ratios are due to mantle CO_2 sources, but without accounting for the range of
157   observed values. While a heterogeneous mantle source is one possibility, other processes such as dissolution
158   in water may also affect CO_2 degassing and carbon isotope composition. If magma bodies in the upper 400 m
159   of the volcanic edifice influence degassing, then we expect compositions of gases emitted above hot
160   intrusions as identified by Zandomeneghi et al. (2013), where a magmatic signature is likely, to differ from
161   those emitted above cooled intrusions, where gases are potentially more deeply sourced but follow old
162   pathways, and are more susceptible to mixing with surface air or dissolution in meltwater.
163
164
165
166   **2. Methods**
167
168   **2.1 Gas sampling**

169   Samples were collected at vents or diffuse degassing sites, within caves and in warm ground areas. We
170   focused on sites that were known to have been entered in the past, due to the biological sensitivity of pristine
171   and little-visited caves. For gas composition, argon and nitrogen isotope analyses, samples were collected in
172   copper tubes and Giggenbach bottles (Giggenbach, 1975). Air samples were also collected inside and outside
173   caves, generally by opening a pre-evacuated vial or Giggenbach bottle. These provide samples for background
174   compositions. Samples for carbon dioxide isotope analyses were taken in 1L Tedlar bags for analysis at the
175   field camp with an infrared isotope ratio spectrometer.
176

177 **Soil probe and titanium tubes**
178   Samples were mostly collected using a 5V battery-powered pump, and a soil probe or titanium tube,
179   connected to sampling vessels by tygon tubing. The soil probe or tube was inserted as far as possible into soil
180   or gravel on the cave floors where temperatures were elevated, or into cracks in the rock where degassing was
181   observed. Typically, sampling vessels included a series of four 30 cm lengths of soft copper tubes with about
182   6 mm internal diameter, linked by short sections of tygon tubing. One end of this sample train was connected
183   to a 1 m soil probe, and the other to the intake of the pump. The pump outlet could be connected to a needle
184   that injected gas through the seal into a pre-evacuated 10 ml glass vial, with a second needle inserted into the
185   seal to maintain gas flow through the vial. In some instances, gas flow out from the vent was sufficient that
186   no pump was required. The highest airflow velocity from a vent was measured by an anemometer at over 6
187     $m \cdot s^{-1}$ (Shooting Gallery, Ice Tower Ridge).
188

189   The pump and soil probe setup was left for several hours, and usually for one day, to flush out ambient air,
190   with the exception of high temperature sites at Sauna and Tramway (measured in 2016) where they were
191   collected after one hour. The battery and pump could operate for several days if required so that samples
192   were not lost in case a return to the site was delayed by bad weather. For collection, we removed the needles
193   from the vial, and cold-welded the ends of the copper tubes while they remained connected to the soil probe.
194

195 **Accumulation chamber**
196   To measure soil CO_2 fluxes, we used a PP Systems accumulation chamber (SRC-1), connected to a portable
197   CO_2 analyser (EGM-4) with an internal pump and rechargeable NiMH battery. The analyser logs CO_2 flux and
198   concentration, and the outlet could be connected to a bag to collect soil gas samples (Lee et al., 2016). The
199   analyser automatically calculates fluxes based on the rise in concentration, for which we specified a linear fitting.
200   We assume there is a linear increase in CO_2 concentration within the cylindrical chamber volume due to
201   constant gas flux. The rate of change in CO_2 concentration over the chamber area (calculated over two minutes
202   for the EGM-4, unless fluxes are high), multiplied by the chamber height then gives the CO_2 flux (Chiodini et
203   al., 1998). Non-linear results generate an error while recording, but wherever all concentration data were saved
204   they have also been checked manually to ensure linear increases in CO_2 concentrations.
205

206 **Tedlar bags**
207   The Tedlar bags used for CO_2 collection and analyses are of impermeable and flexible polyvinyl fluoride, with
208   a plastic valve. Samples in ice caves and warm ground were collected by attaching a bag either to the outlet of
209   the accumulation chamber used for CO_2 flux measurements, or to the outlet of a pump box being used to
210   collect copper tube samples. For lava lake plume and summit fumarole samples, we used 100 mL syringes to
211   draw in air and expel it into the valve, repeating the process several times for each bag, with two samples also
212   collected via the outflow of a MultiGas instrument. These samples are expected to contain a significant
213   proportion of ambient air. Clean ambient air and ambient air next to Lower Erebus Hut (LEH) were also

214   collected using a syringe, while ambient air at Tramway Ridge and within caves were collected by connecting
215   to a pump. Samples were analysed with the isotope ratio spectrometer set up at LEH, usually within 48 hours
216   of collection (section 2.2).
217

218   **2.2 Isotope ratio infrared spectrometer**

219   Carbon dioxide isotope ratios were measured using a tunable-laser isotope ratio infrared spectrometer (IRIS);
220   specifically, the Thermo-Fischer Delta Ray. As in a conventional closed-path infrared spectrometer, the
221   sample gas is passed into an internal cell where it absorbs infrared radiation and the resulting energy spectrum
222   is measured. The absorption wavelengths shift according to the carbon and oxygen isotopes involved, such
223   that peaks on the measured spectrum reflect the proportions of these isotopes. For the Delta Ray, a tunable-
224   laser inside the instrument is the radiation source, targeting the 4.3 μm absorption band. Fitting parameters,
225   including the peaks to be fit, can be specified, and the software uses the HITRAN database (Rothman et al.,
226   2013) as a reference; we used the default settings for CO_2 in air. Using the sizes of and shifts in absorption
227   peaks, the built-in software, Qtegra, calculates the isotope ratios of the sample. The results are referenced to
228   calibration gases of a known composition, which were connected to reference gas intakes and diluted with
229   zero air by the instrument to match the sample concentrations.

230   The instrument was set up inside a hut at Lower Erebus Hut field camp (LEH, elevation approx. 3400 m,
231   ambient air pressure approx. 630 bar). Tedlar bags were connected to the sample intake via tygon tubing and
232   a supplied steel capillary, generally following procedures described by Fischer and Lopez (2016). The sample
233   was pumped into the cell by an internal vacuum pump. To maintain internal cell pressure at the required
234   100.0+/-0.1 mb, an altitude modification was required, in the form of a valve that constricted the tubing
235   between the pump and cell port. For samples containing over 3500 ppm CO_2, dilution was carried out by
236   adding CO_2-free air directly from a cylinder into the bags via tygon tubing. Starting concentrations were
237   estimated from the volume change after dilution, or measured using the Delta Ray before dilution. Due to the
238   possibility of contamination by ambient air during dilution, air sampled near the hut, which is shifted to
239   lighter carbon isotope ratios due to emissions from the stove used for heating, is also reported. Samples were
240   referenced to a Thermo Fisher reference gas with isotope ratios of -27.2 ± 2 ‰ $\delta^{18}O$ and -27.8 ± 2 ‰ $\delta^{13}C$.

241

242   **2.3 Laboratory analyses**

243   Gas compositional analyses were conducted for copper tube, Giggenbach bottle, and some vial samples, in
244   the Volatiles Laboratory at the University of New Mexico following techniques most recently reported by Lee
245   et al.(2017). Splits of the same sample were used for gas chromatography (GC) and quadrupole mass
246   spectrometry. We used a Gow Mac GC with a discharge ionization detector, using a 5Å molecular sieve
247   column with helium as the carrier gas, providing CO_2, $Ar+O_2$, N_2, CH_4, and CO. A Pfeiffer QMS was used in
248   dynamic mode to measure He, Ar, O_2, and N_2. A liquid nitrogen trap was used to freeze out most water
249   before QMS analyses; but as oxygen measurements from the QMS may still be affected by water the results
250   given here use N_2 from the GC, and Ar and O_2 calculated as follows:

251   $Ar_{reported} = Ar_{QMS}/N_{2QMS} * N_{2GC}$

252   $O_{2reported} = (Ar+O_2)_{GC} - Ar_{reported}$

253 Helium amounts in most samples were low (<60 ppm). Argon isotope ratios were obtained by using the
254 QMS to measure masses 36, 38, and 40 in static mode, after a liquid nitrogen trap and a charcoal trap at
255 550°C, following Lee et al. (2017).

256 Compositional analyses showed variability between copper tube samples collected from the same soil probes
257 at almost the same time, which may be due to variations in the level of air contamination. Two possible
258 causes of air contamination are: (1) that air was mixed in during crimping of copper tubes, (2) that cave air,
259 rich in CO_2 and otherwise similar to outside air, is held in the shallow soil and gravel and pumped into our
260 sample set up, but is displaced by intermittent puffs of pristine gas. Most break seal sample splits for nitrogen
261 isotope analyses were therefore prepared from the same copper tubes analysed by GC-QMS. The copper tube
262 was attached to a valve which connected to the vacuum line and a borosilicate break seal at a three-way
263 connection. After evacuating the break seal, a split was taken for GC-QMS analyses, and the copper tube was
264 opened a second time to the break seal to increase the sample pressure, before torching it off. Nitrogen
265 isotope analyses were conducted by isotope ratio mass spectrometry, following de Moor et al. (2013). Air
266 standards in glass break seals were run every 3-4 analyses as references to correct raw values ($\delta^{15}N$ = 0 ‰). A
267 blank was also run for each sample or air standard before breaking it, with the peak areas subtracted from
268 those subsequently measured in the sample or standard run. The blank-corrected air values were subtracted
269 from the blank-corrected sample values. Reported errors are given in 1 s.d. over 4-6 peaks. Although the
270 number of peaks for calculations varies between samples, the same peak numbers were used for the blank
271 corrections and the air standard associated with each sample. Samples collected in 2012 were analysed for
272 carbon and some noble gas ($^3He/^4He$ and $^4He/^{20}Ne$) isotope ratios at the University of Tokyo (Sano et al.,
273 2008)

274

275 **3. Results**

276

277 **3.1 Gas chemistry**
278 Gas analyses from the GC-QMS (Table 1) show that most samples have air-like compositions. The main
279 differences between samples are in their CO_2, O_2, and N_2 contents (Fig 2). Helium is up to a few tens of
280 ppmv above air, reaching 99 ppm for a sample collected at Warren Cave in 2012. Hydrogen (H_2) and
281 methane concentrations are below 0.1%, and CO below 0.2%. Other hydrocarbons may be present, and a
282 fuel-like smell was observed in parts of Warren Cave, but these cannot be measured using our current
283 methods. CO_2 contents are below 2.9%, with four samples containing less CO_2 than ambient air on Erebus.
284 The lowest CO_2/CO ratio measured is 0.5, at Ice Tower Ridge in 2016, while at other sites, CO is not
285 detectable.

286
287 Of the potentially air-derived components, nitrogen varies from about 76% to up to 99%, while oxygen is
288 typically close to or less than 21% down to <1% (with a few samples up to 24%), and argon from 0.5% to
289 1.3%. There is no clear trend in the relationship between these components; low oxygen samples occur across
290 a range of N_2/Ar ratios. High CO_2 concentrations occur both in samples where N_2/Ar and N_2/O_2 ratios
291 resemble air, and in those that are oxygen-poor.

292
293
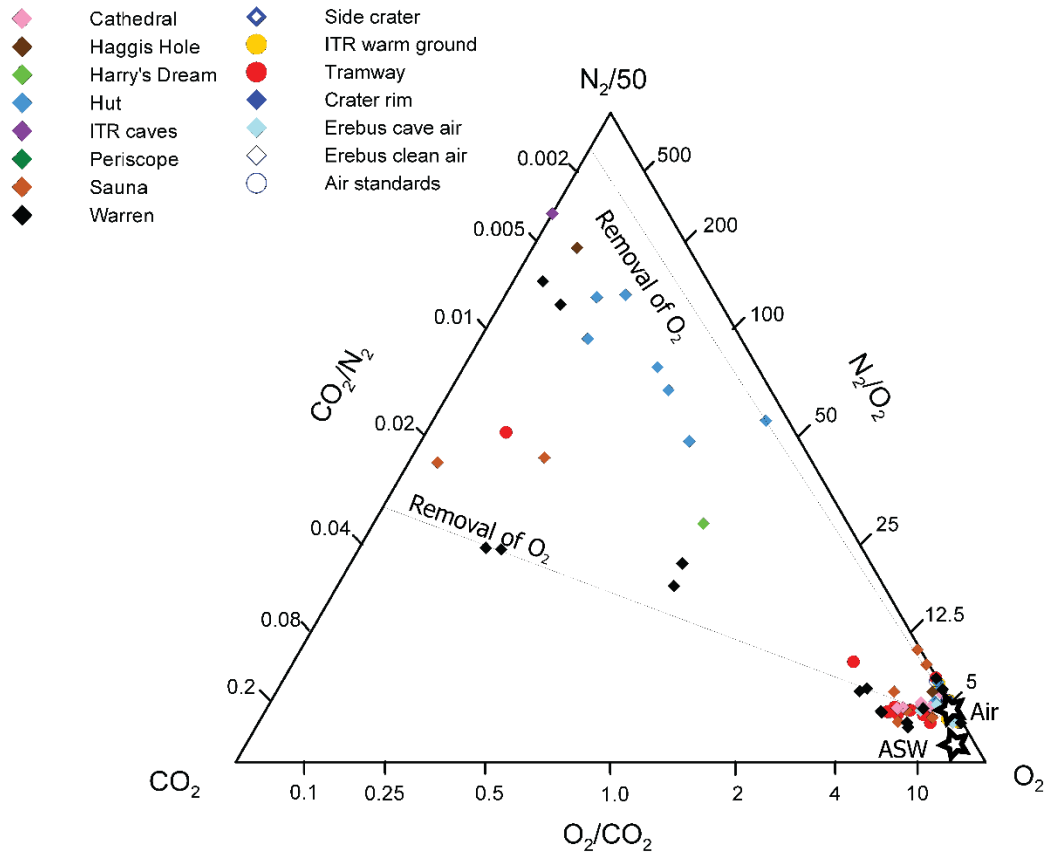
a

b

c

d

295

11
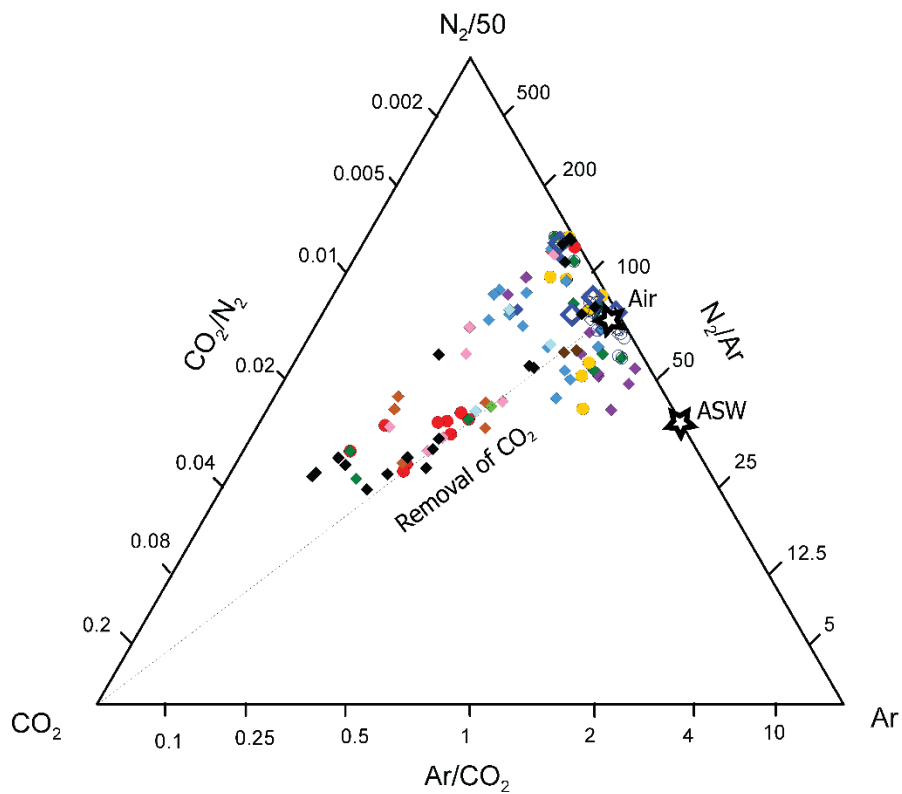
Figure 2. Ternary plots of (a) CO₂-N₂- O₂, (b) CO₂-N₂-Ar, (c) O₂-N₂-Ar, (d) He-N₂-CO₂ measured in 2012, 2015, and 2016 field seasons by GC-QMS.

The samples taken at Hut Cave show that measurements at one site may vary significantly, and as mentioned in section 2, analyses of duplicate copper tubes from the s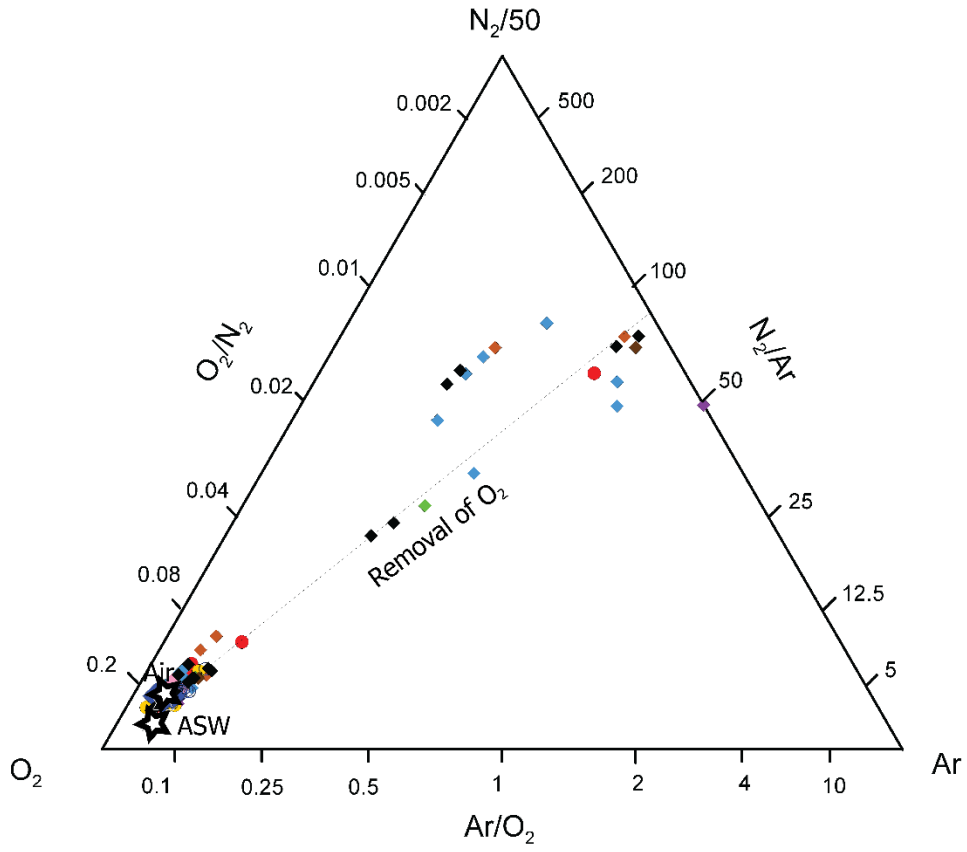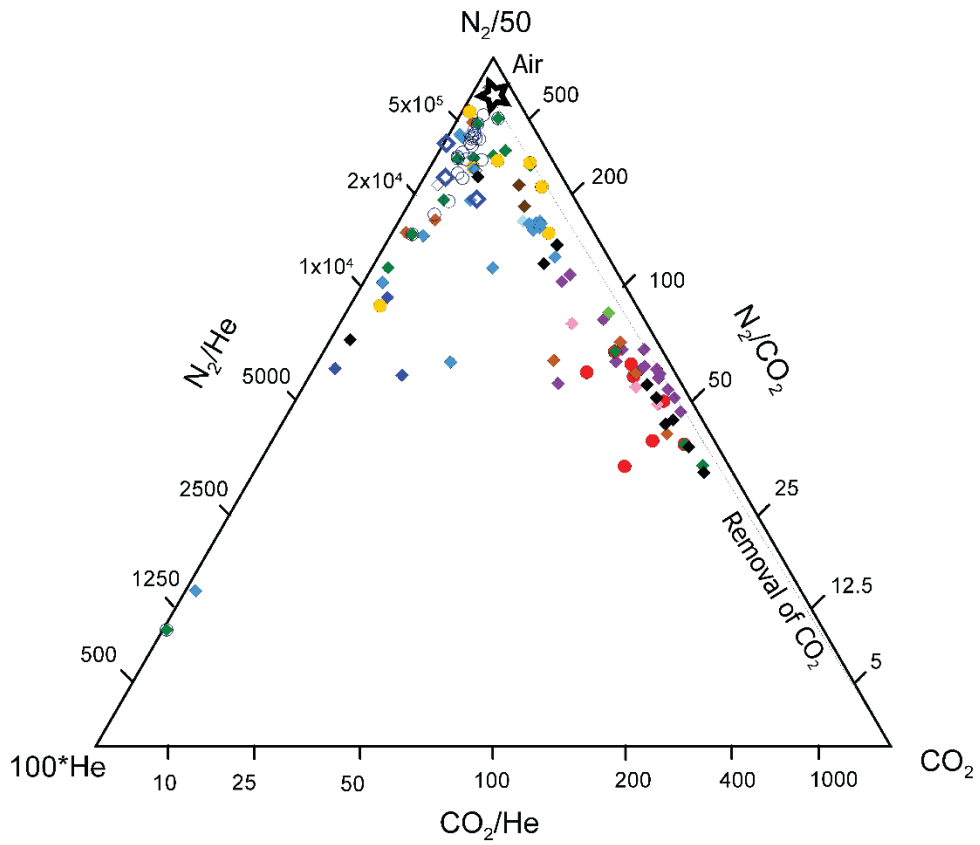ame sampling setup can show differing degrees of air contamination. This includes sites where gas flow out was known to have high CO_2 flux (e.g. Tramway, Sauna) or to be concentrated (such as sites at Ice Tower Ridge and Hut Cave), and we thus consider this to be a result of unsteady flow, at least in some cases, rather than contamination during sampling.

3.2 Isotope ratios

Carbon isotope ratios (Fig 3) are mostly between -2‰ and -6‰. Mixing lines through clean Erebus air or air contaminated by stove exhaust from the hut generally project to a range of values between -1‰ and -4‰ at pure CO_2, and one 2012 sample from Tramway (Table 3) projects to -4.8‰ on a mixing line with 2016 outside air. The time series of samples collected into Tedlar bags at Hut Cave (Fig 4) shows very consistent results, both in concentration and in $\delta^{13}C$ values.
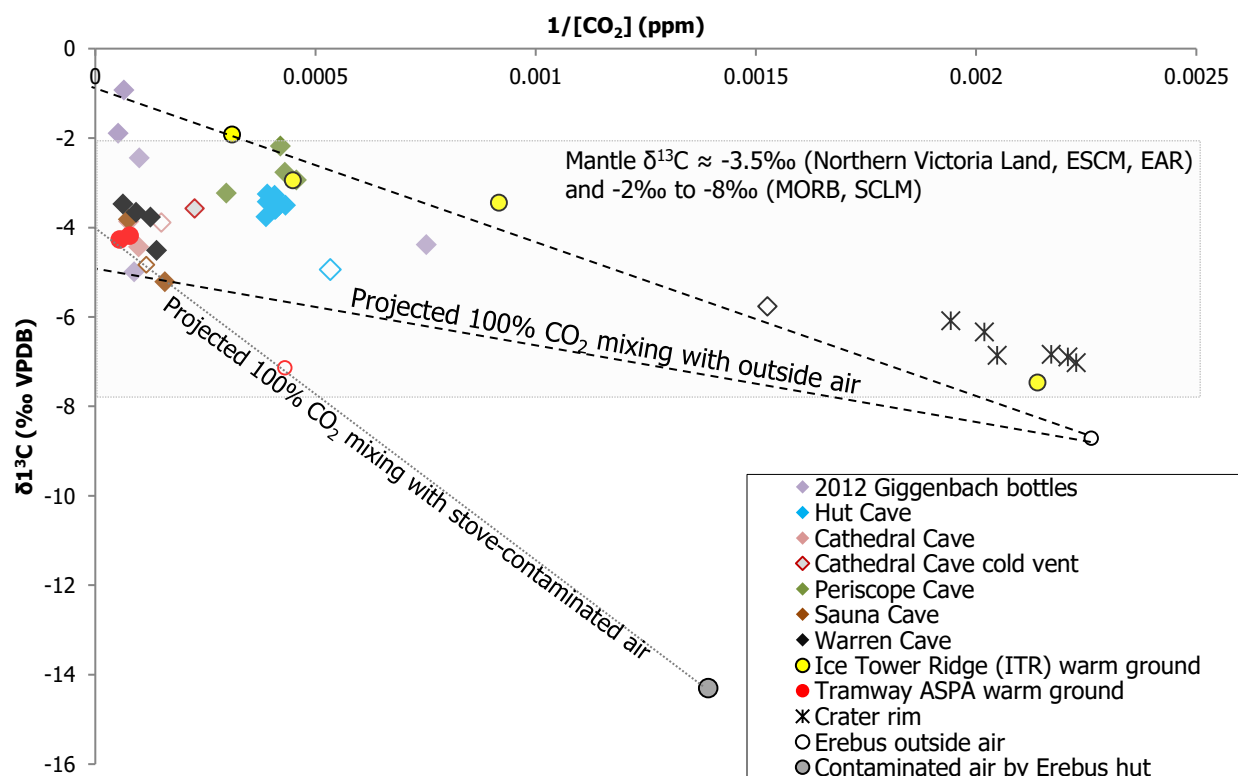
Figure 3. Carbon isotope ratios from Erebus 2016 field season tedlar bag samples measured by Delta Ray, and from 2012 measured by conventional IRMS. Hollow symbols represent ambient air sampled at cave entrances or above warm ground area. Mantle $\delta^{13}C$ are: -3.5‰ for Northern Victoria Land Subcontinental Lithospheric Mantle (Correale et al. 2017), European Subcontinental Mantle (Bräuer et al., 2016), and East African Rift (Lee et al., 2016); -2 to -8‰ SCLM-derived xenoliths (Cartigny, 2005); -5±3‰ MORB (Fischer and Chiodini, 2015)
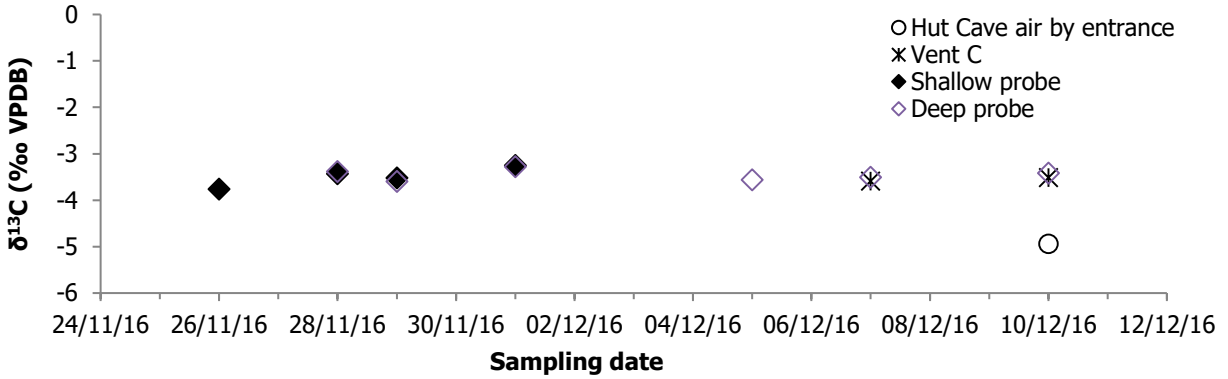
Figure 4. *Time series of carbon isotope ratios collected in Tedlar bags in Hut Cave, measured by Delta Ray*
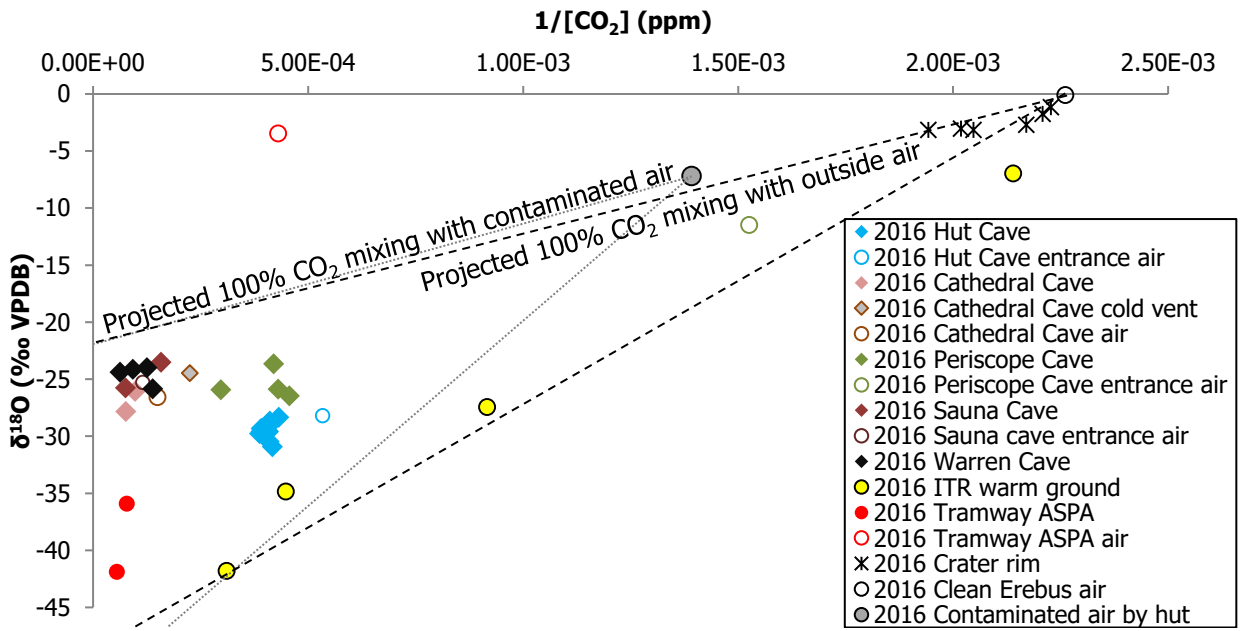
Figure 5. *Oxygen isotope ratios of CO_2 from Erebus 2016 field season measured by Delta Ray. Symbols as for figure 3.*

Oxygen isotope ratios of CO_2 measured by Delta Ray (Fig 5) also vary with $\delta^{13}C$, and lighter oxygen isotope ratios are associated with warm ground areas, while cave vent samples are mostly in the -20 to -30‰ range.
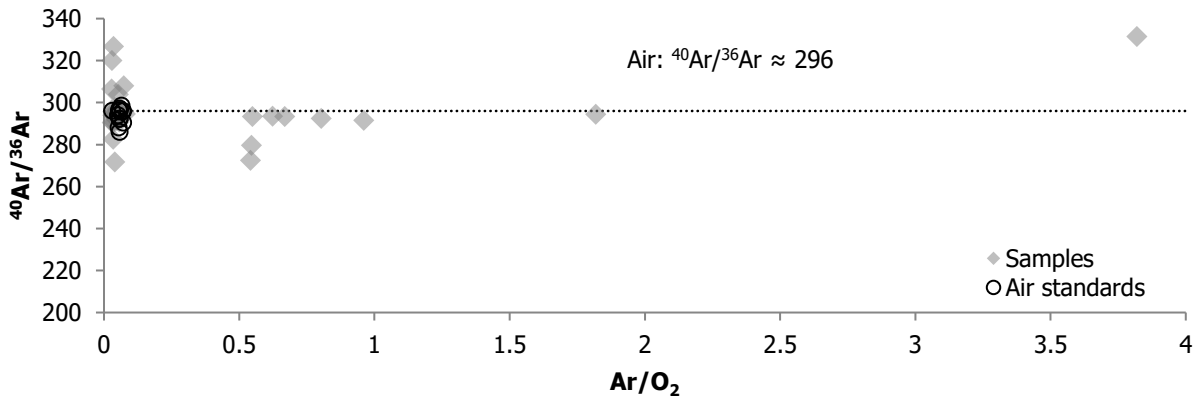
Figure 6. $^{40}Ar/^{36}Ar$ *from 2015 and 2016 samples and laboratory air, measured by QMS.*

13

331

332 Argon isotope ratios (Fig 6), measured on the QMS, range from 272 – 331, which is generally in the range

333 measured for our internal air standard ($^{40}Ar/^{36}Ar$ =286 – 308). The highest value of 331 corresponds to a

334 sample from Hut Cave (HUT-shallow-14), which has the highest N_2/Ar ratio and very little O_2.

335

336

337
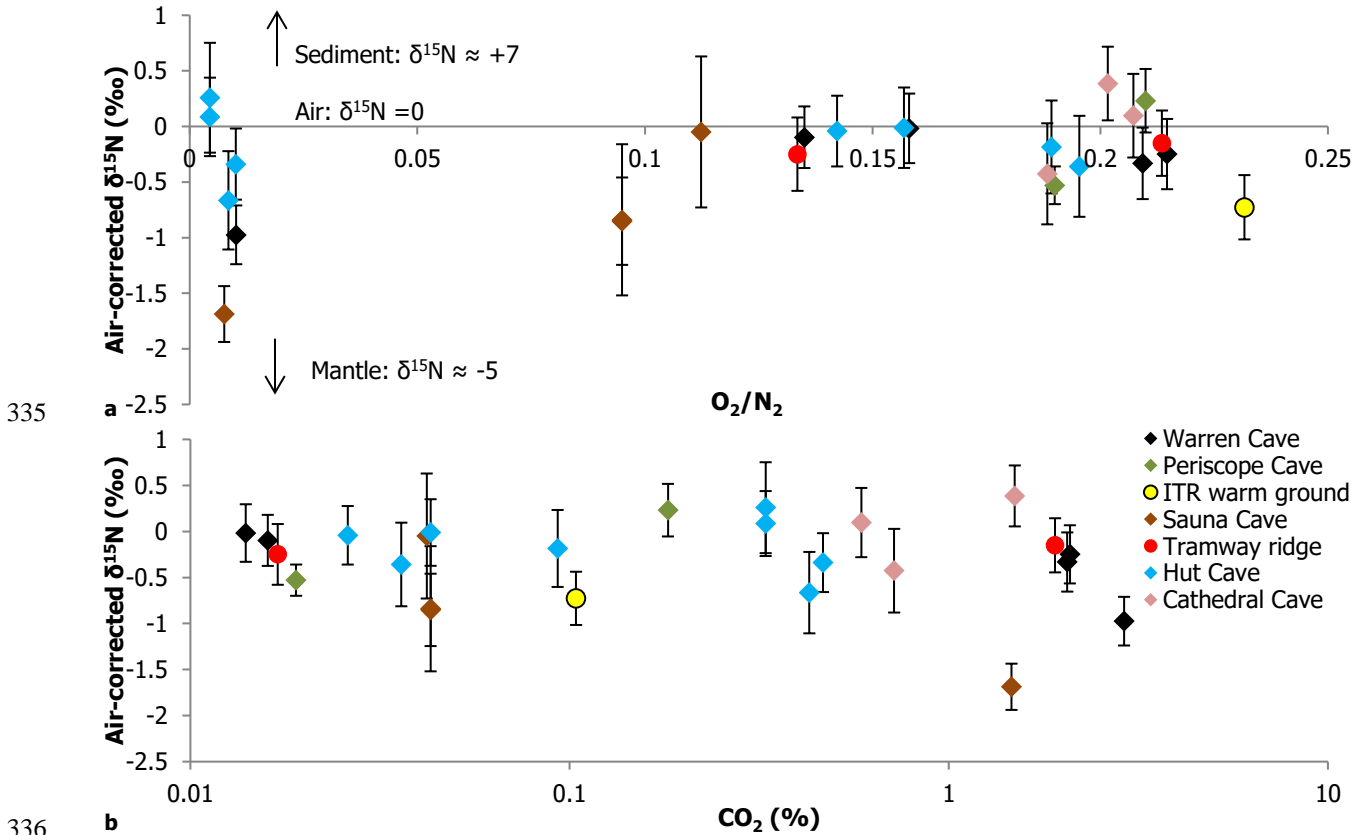
338 *Figure 7. (a) Nitrogen isotope ratios from IRMS vs. O_2/N_2 ratios measured by GC-QMS; (b) Nitrogen isotope ratios vs. CO_2*

339 *(%) measured by GC-QMS. Symbols as for figure 3.*

340

341 Nitrogen isotopes range from -1.7 – +0.4‰ vs air, with 1 s.d. up to 0.6‰ (Table 1, Fig. 7), after recalculating

342 the variance to include standard deviations of air standards used to correct measured raw values from IRMS.

343 The lightest of these values are outside of the range expected for air. Helium isotope ratios (Table 3) are just

344 above those expected for air, with a range of 1.03 – 1.18 R_a.

345

346 *Table 1. Summary of gas data from laboratory analyses (GC-QMS and IRMS); italics indicate ambient air samples (not pumped); < indicates peaks visible on GC but*
347 *amounts below software detection thresholds.*

Type	Sample ID	Site	Gas composition (vol %) from GC-QMS								QMS (static)	IRMS		
			CO_2	He	H_2	Ar	O_2	N_2	CH_4	CO	$^{40}Ar/^{38}Ar$	Sample ID	$\delta^{15}N$	1 s.d.
2012 Cu tubes	EBG-2b	Haggis Hole	0.37	0.0017	0.0005	1.28	0.15	98.20	0.0007	<				
	EBG-20	Sauna	2.09	0.0023	0.0012	1.15	0.16	96.57	0.0005	0.016				
	EBG-14	Tramway	1.08	0.0013	<	0.87	22.33	75.72	0.0011	<				
	EBG-13	Warren v2	0.60	0.0024	0.0004	1.19	0.23	97.99	<	<				
	EBG-9	Warren v5	1.84	0.0013	<	0.90	21.48	75.78	<	<				
	EBG-10	Warren v6	0.06	0.0099	<	0.89	23.42	75.62	<	<				
	EBG-12	Warren v7	2.09	0.0013	<	0.86	23.75	73.30	<	<				
	EBG-11	Warren v8	0.58	0.0015	0.0004	1.23	0.10	98.09	<	<				
2012 Giggenbach bottles w. caustic	EBG-11	Warren v8	0.00	0.0016	<	1.03	13.99	84.98	0.0001	<				
	EBG-9	Warren v5	0.00	0.0013	<	1.06	13.78	85.17	<	<				
	EBG-12	Warren v7	0.00	0.0017	<	1.04	13.79	85.17	<	<				
	EBG-13	Warren v2	0.00	0.0014	<	1.02	14.62	84.36	<	<				
	EBG-15	Harry's Dream	0.00	0.0010	<	1.05	13.62	85.33	<	<				
	EBG-20	Sauna	0.00	0.0016	<	1.03	13.97	85.00	0.0003	<				
	EBG-14	Tramway	0.00	0.0007	<	0.97	13.64	85.39	0.0017	<				
2012 Air standards	*Crest air*	*Sandia crest*	*0.05*	*0.0009*	*0.0006*	*0.97*	*17.67*	*81.31*	*<*	*<*				
	Crest air	*Sandia crest*	*0.06*	*0.0015*	*<*	*0.97*	*17.56*	*81.42*	*<*	*<*				
	Crest air	*Sandia crest*	*0.05*	*0.0012*	*<*	*0.96*	*17.62*	*81.37*	*<*	*<*				
	Crest air	*Sandia crest*	*0.05*	*0.0014*	*<*	*0.94*	*17.46*	*81.54*	*<*	*<*				
2015 Cu tubes	TR1	Tramway	1.47	0.0020	0	1.23	0.41	96.89	0.0020	0.0010				
	HUT1	Hut	0.44	0.0019	0	1.40	0.34	97.82	0.0010	0.0020				
												HUT-2B_2015	-0.184	0.433
	SCR1	Side Crater	0.01	0.0022	0	1.04	18.37	80.58	0	0				
												SCR-2B_2015	-1.488	0.585
	ITR-B-1	Shooting gallery 'blob'	0.05	0.0046	0	0.95	20.06	78.93	<	0				
	ITR-KM-1	Shooting gallery main	0.13	0.0013	0	0.83	20.36	78.67	<	0				
	ITR-UWG-11	ITR upper warm ground	0.02	0.0013	0.0010	0.99	12.56	86.43	0.0010	0.0020				
												ITR-UWG-12_2015	0.0517	0.612
	DDNOS	Hollow near Derodrome	0.15	0.0009	0.0000	1.17	20.89	77.79	<	<				
	ITR-UWG-6	ITR upper warm ground	0.41	0.0012	0	1.42	21.11	77.06	<	<				
	ITR-H-1	Heroin	0.14	0.0013	0	1.01	21.24	77.61	<	<				
												ITR-H-2B_2015	-0.663	0.316
	ITR-LWG-1	ITR lower warm ground	0.29	0.0006	0	1.20	21.35	77.15	<	<				
	ITR-B-6	Shooting gallery 'blob'	0.36	0.0008	0	1.98	0.00	97.66	<	0.0010				
												ITR-B-7A_2015	0.2174	0.122

Group	Sample	Location										Sample		
												ITR-B-7B_2015	-0.797	0.303
	ITR-P-1	Passage by Shooting	0.13	0.0005	0	1.46	20.58	77.83	<	0.0020				
	ITR-TOM-1	Tomato cave	0.06	0.0006	0	1.38	20.91	77.65	<	<				
	ITR-B-16	Shooting gallery 'blob'	0.23	0.0007	0	1.27	21.15	77.35	<	<				
	ITR-B-11	Shooting gallery 'blob'	0.23	0.0005	0	1.23	20.41	78.13	<	<				
	ITR-B-13	Shooting gallery 'blob'	0.23	0.0011	0	1.17	20.94	77.65	<	<				
	ITR-B-A	Shooting gallery 'blob'	0.23	0.0006	0	1.10	19.88	78.79	<	<				
	ITR-UWG-1	ITR upper warm ground	0.23	0.0005	0	1.18	19.80	78.80	<	<				
	ITR-B-12	Shooting gallery 'blob'	0.23	0.0005	0	1.29	18.96	79.52	<	<				
	HUT-3-2015	Hut	0.43	0.0043	<	0.67	0.83	98.06	0.0010	0.0010	292.36	HUT-3_2015	-0.664	0.321
	TR-3-2015*	Tramway	0.02	0.0013	0.0010	0.71	11.69	87.58	0.0020	0.0030	294.97	TR-3_2015	-0.249	0.241
												TR-2B_2015	-0.549	0.278
	ITR-KP-2 2015	Shooting gallery	0.23	0.0014	0.001	0.59	19.11	80.06	<	<	290.42			
	ITR-B-8 2015	Shooting gallery 'blob'	0.34	0.0018	<	0.59	19.18	79.89	<	<				
	ITR_UWG_13 2015	ITR upper warm ground	0.01	0.0026		0.63	15.88	83.47		0.0010				
	SCR_3 2015	Side Crater ice tower	0.05	0.0077		0.59	18.63	80.71		0				
2015 Giggenbach bottles	LEH air 9Dec 15	LEH	0.05	0.0016	0	1.16	18.28	80.51	0	0				
	TR6	Tramway	1.01	0.0032	0	0.92	19.04	79.03	0.0010	0				
	ITR-LWG	ITR lower warm ground	0.09	0.0080	0	0.92	19.37	79.61	0	0				
	SCR8	Side Crater	0.16	0.0025	0.0010	0.89	19.29	79.66	0	0				
	SCR9	Side Crater	0.05	0.0028	0	0.88	19.78	79.28	0	0				
	LEH air 10dec15	LEH	0.04	0.0032	0	0.87	19.30	79.78	0	0				
2015 air standards	Johnson field air	Johnson field	0.03	0.0005	0	1.23	16.43	82.31	0	0				
	Johnson field air	Johnson field	0.04	0.0005	0	1.12	18.21	80.63	0	0				
	Johnson_air	Johnson field	0.03	0.0006	0	1.18	17.44	81.34	0	0				
	Johnson_air	Johnson field	0.03	0.0005	0	1.15	17.64	81.18	0	0				
2016 Cu tubes	HUT-1	Hut	0.11	0.0021	0	0.79	13.71	85.39	0	0	303.82			
	Hut-2*	Hut	0.58	0.0096	<	0.75	1.41	97.25	0	0	279.56			
	HUT-7	Hut	0.39	0.0016	0	0.54	16.70	82.38	0	0	320.09			
	HUT-1-Deep	Hut	0.39	0.0014	0	0.68	17.03	81.89	0	0	326.74			
	HUT-7-Deep	Hut	0.38	0.0014	0	1.26	15.67	82.69	0	0	308.02			
	HUT-14-Shallow	Hut	0.61	0.0018	0	1.56	0.43	97.40	0	0	331.43			
	HUT-Shallow_15*	Hut	0.47	0.0016	0.0020	0.66	0.99	97.87	0.0020	0.0010		HUT-Shallow-15_2016	-	0.236
	HUT_Shallow_16*	Hut	0.04	0.0018	0	0.63	16.24	83.09	0.0010	0		HUT-Shallow-16_2016	-	0.322
	HUT-11-Deep	Hut	0.06	0.0075	0	1.05	15.83	83.05	0	0.0030	294.59			
	HUT-21-Deep	Hut	0.11	NA[1]	0.0070	1.29	1.64	96.89	0	0.0020	272.50			
	HUT-22-Deep*	Hut												
	HUT_deep_23*	Hut	0.33	0.0047	0	0.80	0.44	98.43	0.0010			HUT-deep-	0.0861	0.266
												HUT-deep-	0.2585	0.349
	HUT-27-Deep	Hut									287.29			
	HUT_deep_28*	Hut	0.04	0.0026	0.0010	0.64	13.47	85.84	0.0010	0.0020		HUT-deep-28_2016	-0.011	0.267

	Sample	Location										2016 ID		
	HUT-C-1	Hut - back	0.15	0.0026	<	1.11	20.91	77.82	<	0.0040				
	HUT-C-2*	Hut - back	0.09	0.0049	0.0010	0.61	15.80	83.49	0.0020	0.0010		HUT-C-2_2016	-0.184	0.297
	HUT-C-4*	Hut - back	0.03	0.0019	0	0.66	12.36	86.95	0.0010			HUT-C-4_2016	-0.041	0.245
	CAT-A-1	Cathedral	1.49	0.0028	0.0010	0.67	16.42	81.41	0.0010	0.0010		CAT-A-1_2016	0.3862	0.246
	CAT-A-2*	Cathedral	0.72	0.0014	<	0.68	15.63	82.97	0.0010	<		CAT-A-2_2016	-0.426	0.322
	CAT-B-1	Cathedral	0.59	0.0026	0.0010	0.58	16.97	81.86	0.0020	<		CAT-B-1_2016	0.0969	0.27
	CAT-B-4*	Cathedral	0.10	0.0019		0.64	14.51	84.75						
	ITR-UWG-1	ITR upper warm ground	0.10	0.0020	0.0010	0.73	18.61	80.34	0.0010	0.21	294.84			
	PER-A-2 before torching	Periscope	0.02	0.0018	0.0010	0.59	15.87	83.51	0.0010	0.0010	294.17	PER-A-2_2016	-0.529	0.231
	PER-B-2 before torching	Periscope	0.18	0.0017	0.0010	0.49	17.23	82.09	0.0010	0	306.44	PER-B-2_2016	0.2315	0.229
	Sauna-A-1	Sauna hot vent	0.04	0.0014	0.001	0.64	10.03	89.28	0.0020	<	293.98	Sauna-A-1_2016	-0.049	0.481
	Sauna-A-2*	Sauna hot vent	1.46	0.0018	0.0010	0.68	0.73	97.12	0.0010	0.0020	291.57	Sauna-A-2_2016	-1.687	0.183
	Sauna-B-1	Sauna cool vent	0.10	0.0041	<	0.61	16.35	82.94	<	0				
	Sauna-B-3*	Sauna cool vent	0.04	0.0057	0.0010	0.68	8.61	90.66	0.0010	0.0010	294.55	Sauna-B-3A_2016	-0.852	0.393
												Sauna-B-3B_2016	-0.839	0.281
	Warren entrance air	*Warren*	*0.82*	*0.0030*	*0.001*	*0.56*	*17.18*	*81.43*	*<*	*<*	295.64	ITR-UWG-1_2016	-0.726	0.219
	WAR-v6-1	Warren	2.05	0.0013	0.001	0.56	16.86	80.53	0.001	<	293.97	WAR-v6-1_2016	-0.332	0.246
	WAR-v6-2*	Warren (v6 2012?)	0.05	0.0067		0.61	18.01	81.32			291.13			
	WAR-vT-1	Warren far back	2.81	0.0015	0.0020	0.61	1.11	95.47	0.001	0.0010	293.41			
	WAR-vT-2*	Warren far back	2.09	0.0020	<	0.64	17.19	80.08	<	0	293.32	WAR-vT-2_2016	-0.248	0.224
	WAR-vT-3*	Warren far back	0.01	0.0033		0.66	13.55	85.77			291.60	*WAR-vT-3_2016*	-0.017	0.225
	WAR-CD-1	Warren icy chamber	2.90	0.0013	0.0010	0.61	0.98	95.51	0.0010	0.0010	293.46	WAR-CD-1_2016	-0.974	0.121
	WAR-CD-2*	Warren icy chamber	0.02	0.0037	0	0.66	11.81	87.50			290.74	WAR-CD-2_2016	-0.097	0.506
	TRAM-A-1	Tramway	1.51	0.0012	0.0020	0.64	16.07	81.77	0.0020	<	295.62			
	TRAM-A-4*	Tramway	1.20	0.0012	0.0020	0.88	17.26	80.64	0.0010					
	TRAM-B-1	Tramway	1.91	0.0015	0.0010	0.59	17.16	80.34	0.0090	<	290.21	TRAM-B-1_2016	-0.15	0.221
2016 air standards	*Lab air*	*In lab*	*0.10*	*0.0025*	*0*	*1.31*	*16.58*	*82.01*	*0*	*0*	307.89			
	Lab air	*In lab*	*0.11*	*0.0017*	*0.001*	*1.08*	*16.84*	*81.96*	*0*	*0*				
	repeat	*In lab*	*0.07*	*0.0017*	*0.001*	*1.08*	*16.66*	*82.19*	*0*	*0*				
	Johnson field air	*Johnson field*	*0.08*	*0.0014*	*0*	*1.05*	*18.46*	*80.41*	*<*	*0*				
	Johnson field air	*Johnson field*	*0.08*	*0.0025*	*0*	*1.00*	*18.65*	*80.27*	*<*	*0*				
	Johnson field air	*Johnson field*	*0.08*	*0.0021*	*<*	*0.93*	*16.59*	*82.40*	*<*	*0*				
	Lab air	*In lab*	*0.10*	*0.0033*	*0*	*0.96*	*16.52*	*82.42*	*0*	*0*				
	Johnson field air	*Johnson field*	*0.06*	*0.0015*	*0*	*1.10*	*15.68*	*83.15*	*0*	*0*	295.96			
	Johnson field air	*Johnson field*	*0.06*	*0.0023*	*<*	*1.04*	*16.23*	*82.67*	*<*	*0*	298.60			
	Johnson field air	*Johnson field*	*0.06*	*0.0016*	*0*	*0.98*	*16.98*	*81.98*	*0*	*0*	286.01			
	Lab air	*In lab*	*0.06*	*0.0050*	*0*	*0.56*	*18.61*	*80.77*	*<*	*0*	296.08			
	Lab air	*In lab*	*0.08*	*0.0040*	*0*	*0.98*	*17.63*	*81.31*	*0*	*0*	291.57			
	Johnson Field air	*Johnson field*	*0.06*	*0.0017*	*0*	*1.02*	*17.18*	*81.74*	*0*	*0*	296.37			
	Johnson field air	*Johnson field*	*0.06*	*0.0020*	*<*	*1.01*	*17.33*	*81.60*	*<*	*0*	292.25			
	Johnson field air	*Johnson field*	*0.07*	*0.0015*	*0*	*1.03*	*16.13*	*82.77*	*0*	*0*				

	Sample	Location								
	Johnson field air	*Johnson field*	*0.05*	*0.0023*	*0*	*1.10*	*16.12*	*82.72*	*0*	*0*
	Johnson field air¹	*Johnson field*	*0.04*	*0.079*		*0.70*	*17.89*	*81.29*		
2016 vials¹	*HUT-entrance*	*Hut back*	*0.38*	*0.0013*	*0.0010*	*0.67*	*16.58*	*82.36*	*0*	*0.0030*
	CAT_CaveAir¹	*Cathedral*	*0.94*	*0.0037*	*0.001*	*0.58*	*18.07*	*80.40*	*0*	*0.0030*
	CAT_CV	Cathedral cold vent	0.78	0.0025	0.0010	1.08	16.18	81.95	0	0.0030
	Clean air by Cathedral-	*Outside cave*	*0.11*	*0.0019*	*0*	*0.93*	*23.18*	*75.78*	*0*	*0.00*
	TRAM-A-5	Tramway	1.71	0.0028	0.0070	0.98	18.04	79.26	0	0.0020
	TRAM-B-5	Tramway	1.82	0.0052	0.0010	1.02	17.11	80.04	0.0020	0.0030
	Sauna cave air	*Sauna entrance*	*0.31*	*0.0016*	*0.0010*	*0.90*	*22.91*	*75.88*	*0*	*0.0020*
	Sauna-A-5 vial	Sauna hot vent	2.09	0.0012	0.0010	0.76	20.87	76.28	0	0.0009
	Sauna-B-5 vial	Sauna cool vent	0.82	0.0040	0.0020	0.96	20.24	77.96	0	0.0050
	CAT-A-6 vial	Cathedral	1.49	0.0015	0.0010	1.02	16.58	80.89	0	0.0040
	CAT-B-5 vial	Cathedral	1.30	0.0019	0.0020	1.01	16.32	81.35	0	0.0040
	Vial: ITR-UWG 30 Nov	ITR upper warm ground	0.14	0.0012	0.0010	0.64	23.01	76.20	<	0.0030
	WAR_CD_5_vial	Warren icy chamber	0.07	0.0018	0	0.69	16.48	82.75	0	0
	Sauna_A_good_vial	Sauna hot vent	1.32	0.011	0.0010	0.60	17.29	80.77	<	0.0050
	Low pump site 17:15	*Low pump site*	*0.35*	*0.011*	*0.0010*	*0.69*	*16.73*	*82.21*	*0*	*0.0020*
	Low pump site 17:00	*Low pump site*	*0.08*	*0.013*	*0*	*0.67*	*16.92*	*82.32*	*0*	*0*
	Low pump site 17:06	*Low pump site*	*0.10*	*0.0077*	*0.0010*	*1.10*	*16.43*	*82.36*	*0*	*0.0030*
	Rim after exp 17:15	*Low pump site*	*0.08*	*0.0034*	*0.001*	*1.03*	*16.51*	*82.37*	*0*	*0.0020*
	HUT_5_shallow vial	Hut	0.36	0.0016	0.058	0.98	16.13	82.47	0.0010	0.0020

Table 2. Helium isotope ratios for Cu tube samples in 2012; * indicates duplicates Cu tubes from the same sample setup as the previous sample; ¹ Known or probable helium contamination from GC (copper tubes) or lab air (vials).

Sample location	^{3}He/^{4}He (R_{atm})	^{4}He/^{20}Ne
Harry's Dream	1.10	0.319
Tramway	1.08	0.313
Warren v7	1.05	0.319
Warren v6	1.03	0.316
Warren	1.18	0.320

351 *Table 3. Erebus CO_2 isotope ratios from analyses by IRMS (2012) and IRIS (Delta Ray, 2016)*

Sample ID	Date collected	δ¹³C (‰)	δ¹⁸O (‰)	[CO2] (ppm)
Cathedral				
CAT-cold vent[1]	09/12/2016	-3.57	-24.46	4,440
CAT-cave air[1]	09/12/2016	-3.89	-26.55	6,679
CAT-B-0[1,2]	09/12/2016	-4.43	-26.05	10,210
CAT-A-0[1]	09/12/2016	-3.87	-27.84	13,150
Harry's Dream[3]	2012	-2.44		10,010
Hut cave				
Hut 0 (shallow)	26/11/2016	-3.76	-29.76	2,52
HUT-6 (shallow)	28/11/2016	-3.43	-29.57	2,559
HUT-7 (shallow)	29/11/2016	-3.52	-29.51	2,464
HUT-13 (shallow)	01/12/2016	-3.25	-29.32	2,560
HUT-DEEP-0	28/11/2016	-3.38	-29.31	2,492
HUT-DEEP-1	29/11/2016	-3.60	-29.58	2,452
HUT-DEEP-6	01/12/2016	-3.28	-29.07	2,458
Hut Cave deep site	05/12/2016	-3.56	-29.04	2,438
HUT-DEEP-20	07/12/2016	-3.50	-28.33	2,315
HUT-DEEP-26	10/12/2016	-3.42	-28.68	2,434
HUT-C-0	07/12/2016	-3.59	-30.46	2,441
HUT-C-1[2]	10/12/2016	-3.51	-30.91	2,399
HUT-entrance air	10/12/2016	-4.94	-28.20	1,874
Periscope				
PER-AIR	03/12/2016	-5.77	-11.48	655
PER-A-0	02/12/2016	-2.18	-23.66	2,381
PER-B-0	02/12/2016	-2.77	-25.85	2,324
PER-B-1[2]	03/12/2016	-2.94	-26.46	2,197
PER-A-1	03/12/2016	-3.23	-25.91	3,363
Sauna				
Sauna-A-0[1]	04/12/2016	-3.82	-25.74	13,275
Sauna-B-0[1]	04/12/2016	-5.22	-23.51	6,320
Sauna-entrance air[1]	04/12/2016	-4.83	-25.28	8,660
Warren				
Warren v7[3]	2012	-1.89		19,321
Warren v6[3]	2012	-0.93		15,500
Warren[3]	2012	-4.38		
WAR-CD-0[1,*]	02/12/2016	-3.77	-23.99	8,000
WAR-v6-0[1,*]	30/11/2016	-3.47	-24.38	15,950
WAR-CD-0[1,*]	02/12/2016	-4.51	-25.85	7,200
WAR-v6-1[1,*]	02/12/2016	-3.66	-24.13	10,800
ITR-UWG				
ITR-UWG	30/11/2016	-7.46	-6.96	467
ITR UWG p63[2]	27/11/2016	-2.95	-34.84	2,231
ITR UWG 'fumarole' probe	30/11/2016	-1.92	-41.80	3,223
ITR-UWG p56	26/11/2016	-3.45	-27.44	1,091
Tramway				
Tramway[3]	2012	-4.99		11,386
TRAM-A-0[1]	05/12/2016	-4.18	-35.91	12,795
TRAM-B-0[1]	05/12/2016	-4.27	-41.87	18,160
Tramway air	05/12/2016	-7.14	-3.47	2,322
Rim				
Pump site via pump box 11:45	02/12/2016	-7.03	-1.16	448.9
Pump site via multigas outflow 12:00	02/12/2016	-6.84	-2.70	460.8
Rim - low pump site 16.50	08/12/2016	-6.86	-3.13	488.4
Rim - low pump site 16.58	08/12/2016	-6.34	-3.04	495.4
Rim - low pump site after explosion 17.15	08/12/2016	-6.90	-1.75	452.9
Rim - low pump site after explosion 17.10	08/12/2016	-6.09	-3.14	514.9
Clean air				
CAT-clean air	09/12/2016	-8.71	-0.08	442.3
Contaminated air outside garage				
Outside air	08/12/2016	-14.30	-7.17	718.4

352 * estimated concentration based on dilution volume
353 [1]diluted prior to analysis
354 [2]average of repeat measurements
355 [3]concentrations for samples analysed by IRMS are from corresponding GC-QMS analyses of Giggenbach bottles

19

356

3.3 Carbon dioxide fluxes
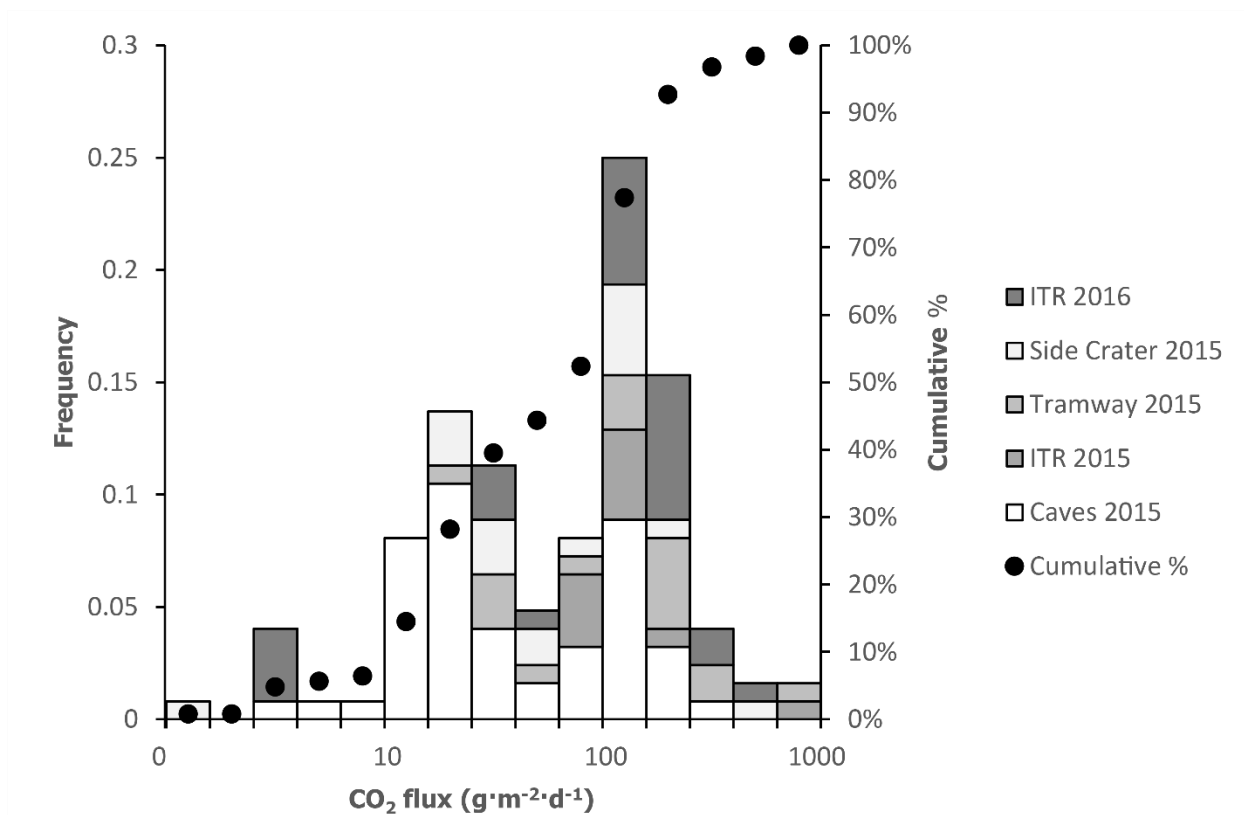
Figure 8. Population distribution of flux measurements taken in 2015 and 2016 at warm ground and cave sites.

Carbon dioxide fluxes measured in caves on Ice Tower Ridge (ITR) and the warm ground areas at ITR, Tramway, and Side Crater, seem to follow bimodal distributions (Fig. 8). Fluxes were estimated for three warm ground sites based on their areas (Table 4), but do not include all such sites on the volcano due to time and access constraints.

Table 4. Summary of estimated CO_2 fluxes from warm ground areas

Warm ground site	Mean flux ($g \cdot m^{-2} \cdot d^{-1}$)	No. points	Median flux ($g \cdot m^{-2} \cdot d^{-1}$)	Area (m^2)	Total emissions (CO_2 $t \cdot d^{-1}$)
Side Crater	119.6	17	74.88	17453[1]	2.09
Tramway Ridge	289.8	17	149.5	17500[2]	4.28
ITR (2015)	199.5	11	149.3	9164[3]	1.83
ITR (2016)	195.8	36	154.6	9164[3]	1.79
All measured (2015)	201.5	45	121.0	44117	8.2

365

[1] From map of Side Crater in Panton and Winter (2008) and field observations

[2] From satellite imagery and Tramway ASPA map (ASPA No. 175 management plan, 2014)

20

370

4. Discussion

4.1 Carbon dioxide

4.1.1 Carbon isotope ratios

374 Previous carbon isotope analyses of gas at Erebus by Wardell et al. (2003) found a range of $\delta^{13}C$ of -2.04‰ to
375 -4.61‰. This was interpreted as an enriched signature from a mantle-derived component with $\delta^{13}C$ of -2.1‰
376 mixed with varying proportions of air. Our measured values overlap with these but have a greater range (-
377 0.9‰ to -5.0‰ before accounting for mixing with air). This matches the -5±3‰ typical of MORB (Fischer
378 and Chiodini, 2015), and the -2‰ to -8‰ range of SCLM xenoliths(Cartigny, 2005), so may reflect a mantle
379 source, but the range of values indicates either heterogeneities in the source carbon isotope ratios, or shallow
380 modification. Fractionation affects the carbon isotope ratios of mantle-derived gases as they travel through
381 the crust, interacting with rock, crustal fluids, and surface air. Additional contributions to CO_2 measured at
382 the surface may also come from mixing, such as with biogenic CO_2, although this is likely to be a minor
383 contribution at Erebus.

384

385 The measurements at Hut Cave (Fig 4) suggest that $\delta^{13}C$ is stable over short time periods (about 14 days) at
386 both sites (Hut Cave main vent and Hut Cave Vent C), with no notable difference corresponding to sampling
387 depth in the soil (Deep probe, Shallow probe).

388

389 We consider scenarios that could determine the range of carbon isotope ratios observed from a combination
390 of source signatures and subsequent fractionation or other modification. We first rule out the possibility that
391 the CO_2 originates from a heavy $\delta^{13}C$ end-member. A heavy end-member would need to reflect the original
392 mantle signature and modification in the crust, prior to shallower processes causing fractionation, to lighter
393 values. At Etna, a similarly heavy end-member is attributed to modification by crustal carbonate sediments
394 (D'Alessandro et al., 1997; Correale et al., 2015). Such an influence is unlikely at Erebus, as there is limited
395 evidence for carbonate basement rock in the crust beneath the McMurdo Sound area (Sims et al., 2008;
396 Fielding et al., 2011; Scopelliti et al., 2011; Phillips et al., 2018), so we consider this improbable. It is more
397 likely that the lighter values reflect an original mantle signature close to MORB values e.g. -4.5 ‰, Cartigny et
398 al. (2001); -5 to -8 ‰, Javoy et al. (1986), or Subcontinental Mantle Lithosphere of around -3.5 ‰ (Bräuer et
399 al., 2016; Lee et al., 2017) and modification is a result of shallow fractionation in the crust.

400

401 We also note that there is potential heterogeneity in the mantle source beneath the WARS. The compositions
402 of Erebus lineage lavas indicate HIMU mixed with DMM type mantle, but their mantle source is considered
403 to be heterogeneous (Sims et al., 2008). Correale et al. (2017) report WARS mantle $\delta^{13}C$ values of -2.5 to -
404 4.5‰ in mantle xenoliths found in Northern Victoria Land. If similar values apply for the Erebus volcanic
405 province mantle, then our measured carbon isotope ratios could be achieved with only minor fractionation.

406

407 However, we do not expect that heterogeneity in carbon isotope ratios at mantle depths could be preserved
408 over very small spatial distances such that distinct $\delta^{13}C$ values were measured at sites only hundreds of metres
409 apart. We therefore assume a lighter source $\delta^{13}C$. An initial $\delta^{13}C$ of -4‰, for example, could cover most of
410 our range of measured values with about +3‰ fractionation. Fractionation processes, such as through

411 magmatic degassing, hydrothermal dissolution, or transport through soil, are the next step in explaining how
412 the measured range of compositions could have been generated.

413

414 Potential influences on the nature and extent of fractionation include (i) the depths and temperatures of
415 shallow degassing magma bodies; (ii) diffusive and advective transport of CO_2; and (iii) the presence and
416 temperatures of any hydrothermal systems, which may relate to the presence of magma bodies and water
417 availability (Table 5). We next consider each of these factors, noting that mixing with non-volcanic CO_2
418 sources would require large quantities of CO_2 with distinct $\delta^{13}C$, and cannot be an important effect here.
419 Although biological and surface air signatures are lighter than mantle, surface air only contributes about 400
420 ppm of CO_2, and with limited biological activity on Erebus, significant microbial CO_2 would be required to
421 alter the isotope ratios of the projected 100% CO_2.

422

423   (i)   Fluxing of CO_2 through the magmatic column is often invoked to explain high CO_2 emissions
424   from Erebus lava lake (Oppenheimer et al., 2011), so the emissions we measure are likely to be
425   sourced from depth, as well as from shallower phonolite magma bodies. Fractionation by
426   magmatic degassing results in lighter carbon isotope ratios.

427 In such a scenario, emissions at Tramway and Sauna cave, and to a lesser extent Cathedral and Warren caves
428 (extrapolated to − 3 to − 4.5‰ at 100% CO_2), would be fractionated to lighter end-members and derive from
429 shallower sources. With a source $\delta^{13}C$ likely close to − 4‰, little fractionation would be required to explain
430 our lightest values. The upper limit on fractionation by magmatic degassing for basalts is well above this, at
431 around -4‰ (Gerlach and Taylor, 1990; Javoy et al., 1978; Mattey, 1991), though no published data are
432 available for basanite, which is the parent melt at Erebus. While degassing pathways are too small to be
433 resolved, Zandomeneghi et al. (2013) do identify larger potential magma bodies at Erebus using seismic
434 tomography. Tramway and Sauna are associated with shallow high velocity zones, i.e. potential hot intrusions,
435 while Hut Cave and Ice Tower Ridge overlie hydrothermal systems or chilled magma bodies. Sources beneath
436 Warren and Cathedral are less clear. The hot intrusions could be a source of gas that has fractionated during
437 magmatic degassing, but this does not account for the heavier $\delta^{13}C$ at other sites such as Periscope Cave or
438 the crater rim. Another mechanism is required for fractionation to heavier values.

439

440   (ii)   Federico et al. (2010) report significant transport-driven fractionation effects during diffuse
441   degassing of CO_2 that can lead to apparent increases in $\delta^{13}C$. This is an important consideration,
442   as there can be fractionation of over 4 ‰ in the interaction between CO_2 and air during
443   diffusion into shallow soil layers(Camarda et al., 2007).

444 This is a difficult effect to evaluate, as many factors may contribute to transport-driven fractionation,
445 including the soil type and CO_2 flux, the pump rate and depth of the sample probe, and wind. The latter is
446 most likely to have affected measurements at Ice Tower Ridge and Tramway Ridge, as these were warm
447 ground areas, exposed to the surface. However, they have very distinct isotope ratios: Tramway Ridge has the
448 one of the lightest of any site (-4.99 ‰), whereas Ice Tower Ridge has a much heavier signature (-1.92 ‰),
449 despite similar exposure to the wind, surface temperatures and sampling methods at both sites. At Hut Cave,
450 sample probes inserted at different depths at the same vent next to one another, and at a second site where
451 gas was blown rapidly out of a crack, yielded very similar $\delta^{13}C$ values after 1-2 days of pumping, suggesting
452 there were no large kinetic effects at shallow depths for that site. We also observe similarities between $\delta^{13}C$
453 measured at different vents within other caves (e.g. Warren, Sauna), despite different rates of gas emission,

454 differing amounts of soil, and different soil temperatures. This does not rule out the possibility of
455 fractionation due to diffuse degassing, and by contrast we do see some variation in $\delta^{13}C$ at Periscope.
456 However, the overall consistency between vents within each sampling site suggests that factors other than
457 kinetic fractionation have a greater role in determining $\delta^{13}C$.

458   (iii)   The shallow plumbing at Erebus may be complex on small spatial scales, as evidenced by the
459 variability of plume gas compositions from its lava lakes ((Oppenheimer and Kyle, 2008)) and
460 changes to summit degassing sites over short time periods. Subsurface magmatic and
461 hydrothermal features could be a factor in the spatial variability of carbon isotope ratios from
462 flank sites. Dissolution of CO_2 in a shallow hydrothermal system and fractionation between
463 dissolved, gaseous, and any precipitating phases (Mook et al., 1974) can cause fractionation.
464 Dissolution in a low temperature hydrothermal system favours lighter values in the gas. This
465 requires temperatures <120°C for HCO_3^-(aq) – CO_2 (g) equilibrium fractionation, or <192°C in
466 the calcite – CO_2 (g) system (Bottinga, 1968; Zhang et al., 1995; Szaran, 1997; Myrttinen et al.,
467 2012). By contrast, dissolution of a light CO_2 end-member in higher temperature systems (i.e.
468 >120°C in equilibrium with aqueous HCO_3^-, or >192°C with calcite) could cause fractionation to
469 heavier values.

472 *Table 5. Properties of degassing sites potentially correlating with measured carbon isotope ratios*

| Site	Seismic tomography[1]	Max vent temperatures[2]	Relative depth[3]	Projected $\delta^{13}C$ (‰)[4]	[CO_2](%)[5]
Tramway Ridge warm ground	LVZ	Hot (59°C)	Surface	-5 to -4	1.3-1.8
Ice Tower Ridge warm ground	HVZ	Hot (59.5^{o}C)	Surface	-1	0.11-0.32
Sauna Cave	LVZ	Hot (43.5^{o}C)	Deep	-4	0.63-1.3
Cathedral Cave	LVZ?	Cool (15°C)	Deep	-3.5	0.67-1.3
Warren Cave	HVZ?	Cool (15.5^{o}C)	Deep	-3	0.7-1.6
Hut Cave	HVZ	Cool (9.7^{o}C)	Shallow	-2	0.24-0.25
Periscope Cave	LVZ	Warm (21°C)	Surface	-2 to -1	0.22-0.34

473 [1]From Zandomeneghi et al. 2013. [2]Hottest vent temperatures at sample sites in this study. [3]Relative to local ground surface. Periscope cave is largely
474 horizontal, while the vents in Hut Cave are below ground surface (approx. 2-4 m). Warren, Cathedral-Mammoth, and Sauna, all have entrances over 10
475 m below the surface ice. [4]See figure 3 for projected mixing lines. [5]Concentrations for Warren, Tramway, and Sauna are estimates; those for Cathedral
476 were measured directly by Delta Ray before dilution. Hut, Periscope, and ITR concentrations could be measured directly during the Delta Ray
477 analyses.

479 The highest outlet temperatures (59°C) were observed at both Tramway and ITR warm ground sites, which
480 bracket the measured range of carbon isotope ratios. The difference between the two could be explained by
481 the presence (ITR) or absence (Tramway) of a high temperature hydrothermal system. If we assume
482 fractionation solely between dissolved bicarbonate – gaseous CO_2 and take Tramway to represent the
483 unmodified magmatic and most mantle-like gas, fractionation factors suggest a temperature of about 200°C
484 could give a +4‰ heavier $\delta^{13}C$-CO_2 (Myrttinen et al., 2012), accounting for maximum projected difference
485 measured at ITR compared to Tramway. Lower temperature systems would experience less fractionation,
486 explaining the intermediate values observed at Hut and Periscope caves. Carbon dioxide dissolves more
487 readily into aqueous solutions at low temperatures (Lowenstern, 2001), so that lower fluxes are also expected

488 above low temperature hydrothermal systems. This may account for small difference in fluxes between
489 Tramway and ITR, and high CO_2 concentrations in bag samples at Tramway compared to ITR or the caves.
490 Samples from the crater rim also have a heavier $\delta^{13}C$ signature despite CO_2 concentrations being close to air.
491 This could result from removal, through dissolution, of magmatic CO_2, combined with fractionation in a high
492 temperature hydrothermal system similar to what we propose beneath ITR.

493 The source of hydrothermal water is likely meteoric, but the depth at which the interaction with magmatic gas
494 begins is unknown. The water source is important in considering whether it is plausible that the CO_2
495 emissions at Periscope (-2 to -1 ‰) could be affected by hydrothermal interactions without any similar effects
496 nearby at Tramway (-5 to -4 ‰). Localised melting is observed within caves, and refreezing results in the
497 increased ice density measured by Curtis (2015). Periscope and Hut caves, where surface snow is frequently
498 blown in to the caves, have heavier projected $\delta^{13}C$ (-2 to -1‰) than the deeper Sauna, Warren, and Cathedral
499 caves. This might suggest that gases emitted from shallow caves are more influenced by shallow percolation
500 of meltwater and isotopic fractionation due to dissolution, but only if meltwater could reach sufficiently high
501 temperatures to cause fractionation to heavier $\delta^{13}C$. We do not have enough evidence to determine whether
502 ice thickness or proximity to the base of the snowpack might influence degassing. In addition to melting in
503 the summit area, if a larger subglacial groundwater system (Flowers, 2015) were to exist beneath the lower
504 glaciated flanks of Erebus, there could be a more extensive hydrothermal system circulating to greater depths.
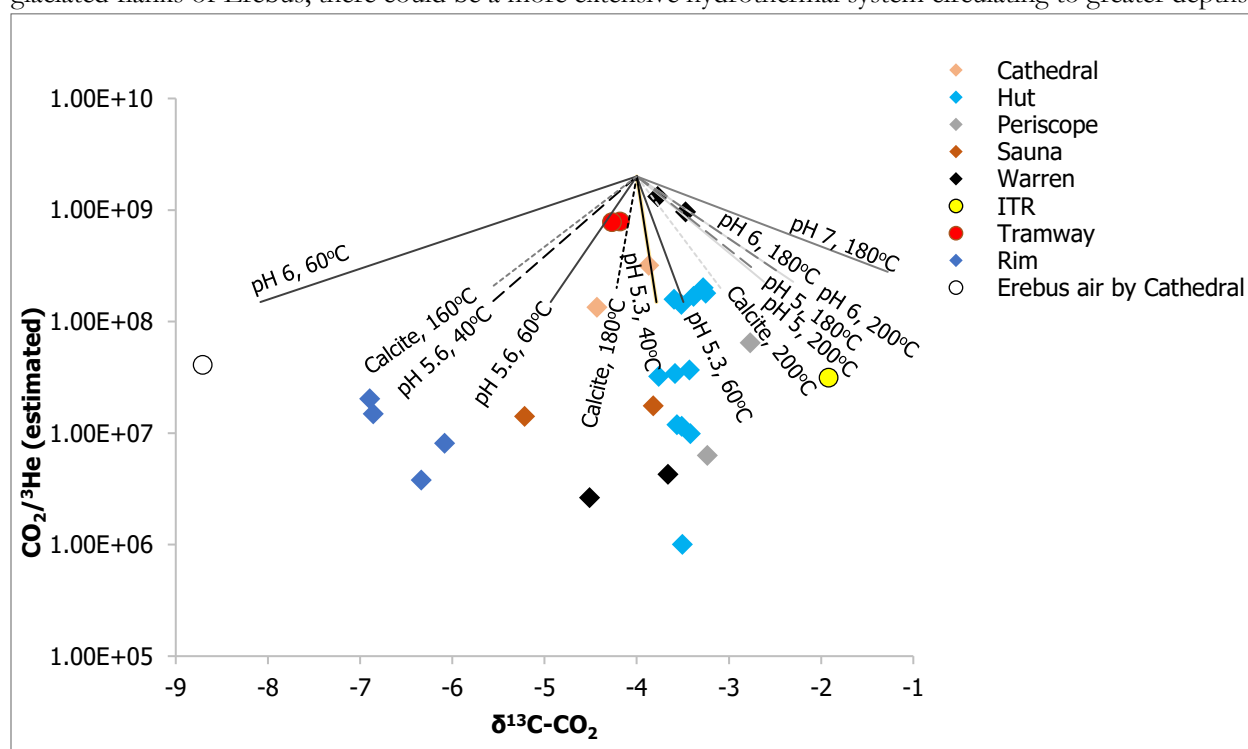
505

506 *Figure 9. Possible fractionation pathways from partitioning of CO_2 (g) in water with precipitated calcite or aqueous HCO_3^- and*
507 *H_2CO_3, which is pH dependent. $CO_2/^3He$ ratios are from GC-QMS measurements of CO_2 and total He, with ^3He estimated*
508 *from a constant R/Ra, assumed to be 1.18, from IRMS analyses of 2012 copper tube samples. The fractionation lines start*
509 *from an assumed $CO_2/^3He$ of 2x10⁹, which are likely values for DMM and MORB (Resing et al., 2004; Barry et al., 2014)*
510 *as well as close to the lower values found by Barfod et al. (1999) for gases from the Cameroon volcanic line. They are calculated*
511 *up to a dissolved CO_2 fraction of 93% or precipitated calcite of 90%.*

512   For Rayleigh fractionation of CO_2 dissolving in water, with partitioning between CO_2 (g) and calcite or
513   HCO_3^- (aq), using fractionation factors from the literature (Malinin et al., 1967; Clark and Fritz, 1997), we can
514   consider the range of concentrations and $\delta^{13}C$-CO_2 that could be generated by fractionation in a
515   hydrothermal system. Using CO_2/He ratios from GC-QMS analyses, and assuming a constant R/Ra, of 1.18,
516   which is the highest measured from our samples, we follow Gilfallan et al. (2009) to plot estimated CO_2/^{3}He
517   vs $\delta^{13}C$ (Fig. 9). We see in Figure 9 that direction of fractionation is influenced both by temperature and pH,
518   with fractionation to heavier carbon isotope ratios in the discharging CO_2 requiring high temperatures or
519   lower pH. With calcite precipitation, still higher temperatures are required, as the crossover point when $\delta^{13}C$-
520   CO_2 begins fractionating to heavier values is at around 192°C (Malinin et al., 1967). We consider the range of
521   carbon isotope ratios that can be generated with slight variations in temperature or pH conditions to support
522   hydrothermal fractionation at Erebus. The mechanism for CO_2 loss and the water pH would be required to
523   constrain the temperature. Regardless of these, however, CO_2 loss of over 99% of the original gas is required
524   to reach the measured amounts. The most likely scenario, therefore, is dilution and removal of CO_2, through
525   air mixing combined with dissolution in a high temperature or slightly acidic hydrothermal system.

526

527   *4.1.2 Oxygen isotope ratios*
528   Attempts to calculate the original oxygen isotope ratios of any water in equilibrium with the measured CO_2,
529   following Chiodini et al. (2000) are prevented by the lack of constraints on equilibration temperatures and
530   H_2O/CO_2 ratios. Sample temperatures are relatively low, and equilibrium is likely to be with liquid water
531   where it is present. The more dilute samples from the crater rim resemble air, which is consistent with the
532   rapid kinetics of $\delta^{18}O$ equilibration between CO_2 and H_2O, whereas the lightest oxygen isotope ratios are at
533   Tramway Ridge and ITR, where steaming ground indicates water emissions. We did not collect snow samples
534   from the same sites for oxygen isotope data, but our warm ground data may be consistent with CO_2 re-
535   equilibration to Erebus snowmelt with light $\delta^{18}O$ due to the altitude (Assonov et al., 2005). The cave samples
536   and cave air fall in an intermediate region, likely indicating a combination of meltwater and air contamination,
537   rather than a heavier magmatic water component. The higher temperature fumaroles in the main crater, and
538   the concentrated plume closer to the lava lake, could not be accessed, but in theory could provide more
539   reliable constraints on oxygen isotopes in combination with $\delta^{18}O$-H_2O from snow (e.g. Curtis, 2015).
540

541   *4.1.3 CO_2 flux and concentration*
542   Direct flux measurements at Side Crater, Ice Tower Ridge, and Tramway range from around 120 – 290 g·m^{-2}·d^{-1}
543   with a total of about 8.2 t.d^{-1}. This is lower than the flux estimated for total flank degassing by Wardell et
544   al. (2003), who quantified fluxes out of openings on ice towers and caves as well as warm ground, and found
545   higher fluxes overall, totalling 40 t.d^{-1}. Their method was based on fewer measurements over a greater area
546   and it is likely that our measurements did not cover the same areas. We included Side Crater, which was not
547   in their study, whereas they report higher fluxes on upper Tramway Ridge (4760 g.m^{-2}.d^{-1}), suggesting that our
548   coverage of Tramway was different or that fluxes have changed. Soil degassing at the ITR site appears
549   consistent between our measurements in 2015 and 2016, suggesting stability over these time periods. The
550   CO_2 concentrations from GC-QMS analyses do not exceed 2.9%, which is consistent with amounts measured
551   by Wardell et al. (2003).

552

553   If we assume that the difference in CO_2 fluxes between Tramway and ITR is due to a 200°C hydrothermal
554   system beneath ITR dissolving CO_2 as bicarbonate, we can use the solubility of CO_2 in water to calculate that
555   the approx. 44 g·m^{-2}·d^{-1} that is lost must be interacting with a 6.5 x 10^6 L volume of water per day. Given our

556 estimates of the surface area at ITR (9164 m^2), this could suggest an aquifer thickness of 2 – 14 m depending
557 on capacities of 5 – 33% water for the aquifer.

558

559 Our attempts to quantify diffuse CO_2 flux in caves were complicated by high CO_2 content in the cave air,
560 which often prevented accurate flushing of the accumulation chamber. In these cases, cave air CO_2 exceeded
561 that measured in samples from the ground. Constant high gas flow may be responsible for more established
562 deep caves at Warren and Cathedral.

563

564 Our flux measurements fall into two broad populations (Fig. 8), the reason for which is not clear.
565 Hydrothermal dissolution of CO_2 cannot account for the CO_2 flux population distributions, as Tramway and
566 ITR have similar distributions, although they have different overall fluxes and carbon isotope ratios that are
567 consistently different. In addition, although CO_2 solubility in water decreases with temperature, ITR has
568 similar or lower concentrations of CO_2 in the sampled gases compared to Hut and Periscope, despite a
569 projected higher temperature hydrothermal system based on its heavier carbon isotope ratios. Combined with
570 the observation that low CO_2 concentration samples have more air-like carbon isotope ratios, this makes it
571 more likely that the degree of air contamination is responsible for the observed CO_2 flux distribution, i.e.
572 lower fluxes could be associated with a higher proportion of atmosphere-derived air.

573

574 **4.2 Gas compositions and atmospheric air**

575 Most copper tube and Giggenbach bottle samples are dominated by air (Fig. 2, Table 1). This could be due to
576 contamination during sampling, mixing with cave air before sample collection, recirculation of air through the
577 volcanic edifice (e.g. Bergfeld et al., 2015), or incorporation of air into the convecting lava lake at the summit
578 followed by transport from the degassing magma to the ice caves.

579 If gas flow out of vents is unsteady, pumped samples may contain cave air mixed with occasional pulses of
580 more deeply-sourced gas, which could explain why copper tube sample compositions are variable. This
581 variability may not be picked up over the area and timescales of the flux meter measurements or in collecting
582 1 L of sample for carbon isotope measurements. The nitrogen-rich samples could then represent either a
583 magmatic end-member, or an air-contaminated CO_2 rich gas with oxygen removed (Fig. 2a). Airflow
584 resonance in caves is a recognized phenomenon (Cigna, 1968) that may result in high frequency periodicities
585 in CO_2 concentrations (Faimon et al., 2012). Such observations have focused on cave air and air at cave
586 entrances, but we speculate that similar processes on a smaller scale may affect compositions between
587 duplicate copper tubes at cave vents.

588 Air contributions to vent degassing could also result from more systematic incorporation of atmospheric air
589 via caves or permeable volcanic rock and soil. Mechanisms for this could include differential air temperature
590 or pressure, or wind -driven mixing. Barometric pumping occurs at Warren Cave, and seems to only affect
591 the degree to which air is pulled out of ice towers and caves (Curtis and Kyle, 2011). However, there are other
592 drivers of circulation that have been identified both in caves and on mountain slopes: the temperature-driven
593 chimney effect, with cold air pulled in at lower entrances and warm air emitted at higher ones, and 'mountain
594 breathing' caused by wind (Woodcock, 1987). These can occur in porous soils even in the absence of caves or
595 volcanic degassing (Thorstenson et al., 1998; Bergfeld et al., 2015). At Erebus, fractures in the ice cover on
596 the lower flanks, for example at glacial crevasses, and exposed rock or soil in the summit caldera, could
597 permit atmospheric air into the edifice. Emissions of CO_2 in such instances could also be affected by

598   atmospheric conditions and wind-driven circulation (Lewicki et al., 2007; Ogretim et al., 2013). The lava lake
599   is open to the atmosphere and is another potential site for mixing; however, entrainment of cold air at lower
600   levels, rather than at the summit where hot gas is also emitted, is more consistent with the chimney effect.

601   The N_2/Ar and O_2/Ar ratios of gas samples tend to be within the ranges measured for air samples. The
602   N_2/O_2 concentrations, however, range from air-like to having O_2 below detection. In N_2-Ar-O_2 space the N_2-
603   O_2 and Ar-O_2 variations are linear, implying that the nitrogen-rich gas results from oxygen being removed
604   without affecting the N_2/Ar ratios, rather than from magmatic gas containing excess nitrogen mixing with air
605   (Fig 2c).
606
607   An additional mechanism for modifying air or magmatic gas is dissolution in hydrothermal waters, which is
608   likely to have affected carbon isotope ratios through dissolution of CO_2. Similar fractionation can occur
609   between gases. The solubility of CO_2 in neutral waters is much higher than that of Ar and O_2, which have
610   similar solubilities, while N_2 is less soluble (Sander, 2015). We can calculate the ratios of these species in
611   equilibrium with the exsolved gas at changing temperatures, assuming some initial ratios and temperatures
612   (Fig 10).
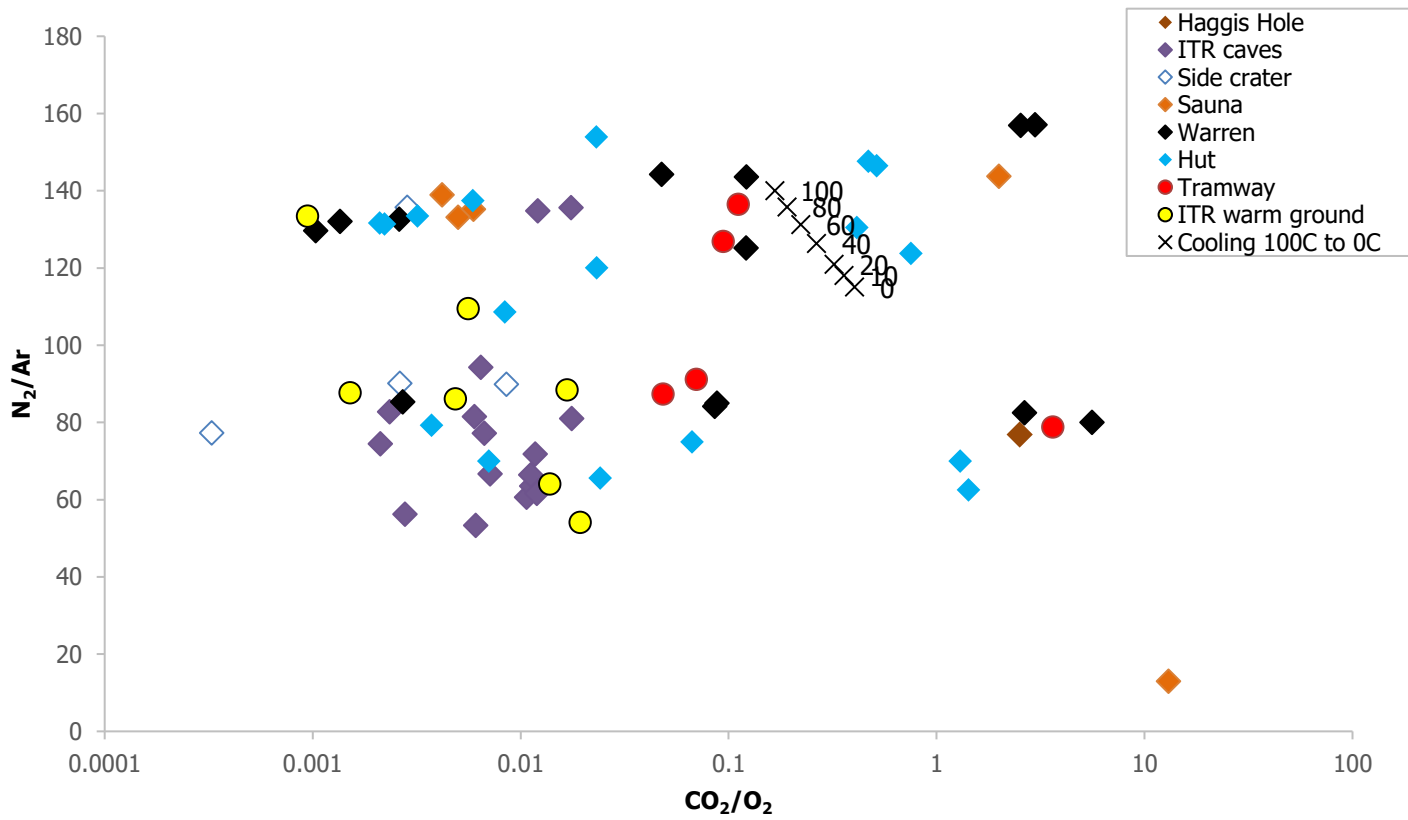
613
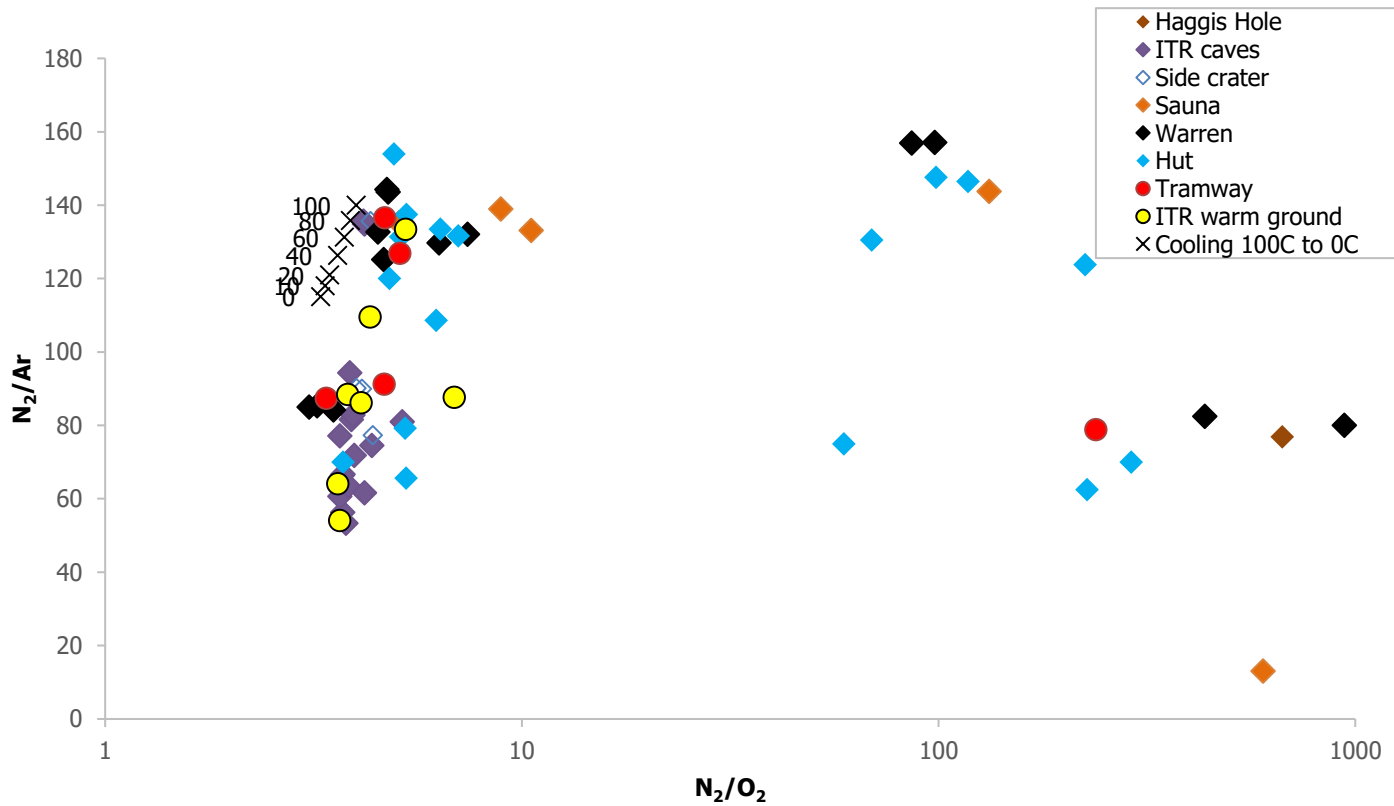
614

615   *Fig 10. Examples of projected gas ratios from dissolution and re-exsolution of gas ($N_2/Ar = 83$, $N_2/O_2 = 4$, $CO_2/O_2 =$*
616   *1.7) in water cooling from 100 to 0°C (Henry's Law constants from Sander 2015). Labels indicate temperature of the water.*

617 *from which degassing occurs. The range of these ratios produced in this way is smaller than observed in our gas samples,*
618 *particularly compared to the spread of the x-axis.*
619
620 The difference between measured gas ratios and those of the same species dissolved in pure water is at a
621 maximum at 0°C. At higher temperatures, this difference decreases, so re-exsolution from cooling water
622 could account, for example, for increasing CO_2/O_2 or decreasing N_2/Ar ratios (Fig 10). However, the
623 measured range of ratios is far greater than the maximum fractionations indicated by these calculations.
624 Despite the similarity in solubilities between Ar and O_2, the spread of N_2/O_2 is much greater than that of
625 N_2/Ar and cannot be explained by gas dissolution and re-exsolution. In the following sections we show that
626 oxygen removal, rather than a high nitrogen content, is also supported by $\delta^{15}N$ and argon isotope data.
627
628 This is also consistent with the relationship between CO_2 and N_2/Ar (Fig. 2b). An initial magmatic gas can be
629 partially stripped of CO_2 in a hydrothermal system. Mixing a small fraction of this gas with air would not
630 noticeably affect N_2/Ar, given that mantle, ASW, and air values for N_2/Ar are relatively close. Oxidation of
631 the surrounding rock could lead to an oxygen depleted air-like composition, potentially retaining some CO_2
632 whose carbon isotope composition reflects hydrothermal interaction. Combustion at the lava lake surface
633 would be a second mechanism to remove oxygen, where magmatic gas could mix with oxygen-depleted air
634 from the surface. However, we suggest that the first scenario is more likely given that pulling such significant
635 proportions of cold air into the lava lake is counter to the chimney effect. We speculate that there is a further
636 possibility of interaction between air and magmatic gases at high temperatures (Martin et al., 2006) but at
637 greater depths in the plumbing system, rather than at the lava lake. Oxidation by reaction between air and
638 magmatic gas rather than rock could also remove CO and H_2 (Giggenbach, 1987), accounting for the low
639 proportion of these species in our samples, though oxidation of CH_4 by oxygen will be slower (Li and
640 Hoflund, 2003). Regardless of the mechanism for oxygen removal, the variability in oxygen content between
641 samples collected in the same time periods also shows that air mixing occurs throughout the system. This
642 could be due to unsteady supply of a magmatic-hydrothermal gas that has been stripped of oxygen, or to
643 variations in the amount of air added subsequently.
644
645 **4.3 Nitrogen and argon isotopes**
646 Variations in $\delta^{15}N$ are small. Most samples are air-like, consistent with N_2/Ar ratios. A range of about -1.5 –
647 0.5‰ suggests a minor contribution from a MORB-type mantle component. Projecting a mixing line between
648 air and the lightest samples towards $O_2/N_2 = 0$ gives a nitrogen isotope ratio of about -1.8‰, somewhat
649 heavier than commonly cited MORB mantle values (Marty and Zimmermann, 1999; Mohapatra and Murty,
650 2004). We consider this to be the closest to source values, as kinetic fractionation during open system
651 magmatic degassing is unlikely (Fischer et al., 2005) and would occur alongside fractionation of $\delta^{13}C-CO_2$
652 (Cartigny et al., 2001).
653
654 A three-component mixing model (Fig. 11) can be used to examine the likely contributions from mantle, air
655 or air-saturated water (ASW) at 0°C, and sediment sources, following Sano et al. (2001). The $N_2/^{36}Ar$ values
656 here are derived from the average $^{40}Ar/^{36}Ar$ of 294.07 of our data. This shows that most of our data can be
657 explained by mixing between a mantle end-member and air. As described by Sano et al. (2001), the mixing
658 equations can be used to calculate the contributions of each end-member. Some samples (HUT1, ITR-UWG-
659 11) resemble air despite being emitted at higher than ambient temperatures. The highest potential mantle
660 contribution is from Sauna cave (Sauna-A-2) where 38 % (if mixed with air) to 57% (mixing with ASW) could
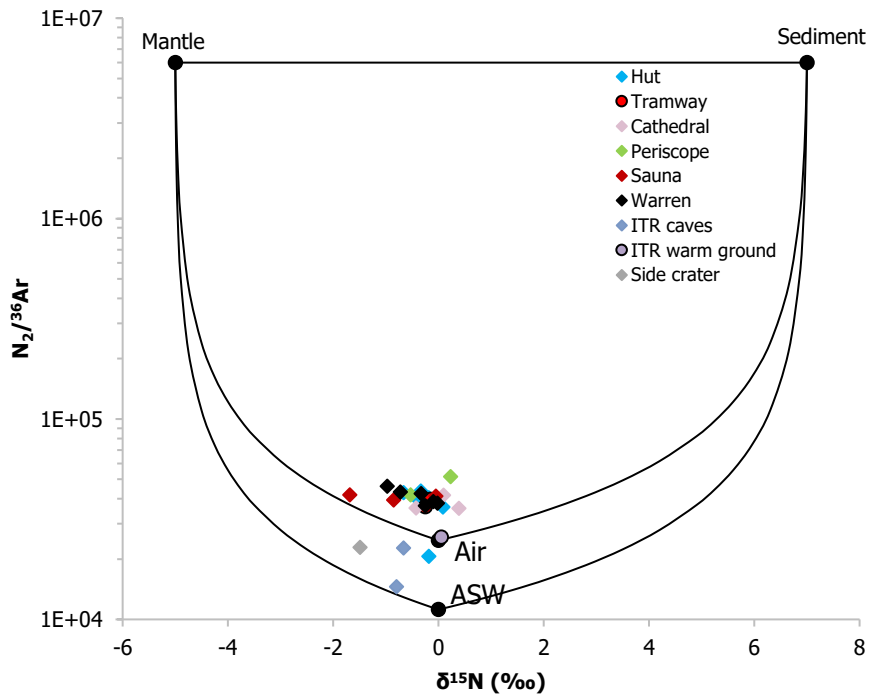661 be mantle-derived.

Fig. 11. $N_2/^{36}Ar$ vs $\delta^{15}N$ using ^{36}Ar from argon content in each sample and average $^{40}Ar/^{36}Ar$ ratio of all samples analysed for argon isotopes (294.1), following Sano et al. (2001).

However, an alternative possibility to mixing is that fractionation of nitrogen between gas and dissolution in water is responsible for the variation in isotope ratios. Experiments by Lee et al. (2015) measured fractionations from +0.91‰ for N_2 dissolved in water at 5°C to -0.42‰ at 60°C, with a crossover at 40°C. Regardless of whether fractionation or mixing are responsible for the range of $\delta^{15}N$, the samples from Sauna Cave with the lightest nitrogen isotope values and highest temperatures are the least modified by atmospheric air contamination or dissolution and exsolution from the original magmatic gas.

Samples from sites other than Sauna Cave, even where N_2/O_2 ratios are high, have more air-like $\delta^{15}N$. This indicates that the process by which N_2/O_2 is increased is independent of the nitrogen source; oxygen is removed from gases that are predominantly air as well as from those that contain a greater mantle-derived component. Argon isotopes are also air-like, with one relatively argon-rich sample (HUT-shallow-14) having a slightly higher than air (295) $^{40}Ar/^{36}Ar$ of 331.

These stable isotope ratios indicate a primarily air-derived gas, which requires a mechanism for removal of oxygen rather than the addition of nitrogen. As discussed in the previous section, removal of O_2 by dissolution in water would similarly affect Ar and is inconsistent with observed trends shown in Figures 2 and 10. Another mechanism is a redox reaction with gas or rock that removes oxygen from air. Examples might be reactions with and removal of reduced gas species such as CO, H_2, H_2S, and CH_4. Of these species, reaction of hydrogen sulfide with iron in rocks may account for sulfur species not being detected in flank degassing (Symonds et al., 2001). The remaining species are only observed in trace amounts in our samples. A more likely scenario is reaction of O_2 with rock close to the surface, resulting in oxidation of the rock and removal of O_2. A final possibility is that microbial oxidation sometimes exceeds the supply of oxygen from atmospheric air. At Warren and neighbouring caves, biological studies have found CO oxidizing bacteria

30

689 (Tebo et al., 2015), but this cannot account for gas compositions that seem only to have oxygen removed,

690 without increased CO_2. Some combination of these processes may be responsible for oxygen depleted gases.

691

692 **4.4 Degassing model and implications**

693 Figure 12 shows likely pathways contributing to the upper flank degassing of Erebus, with mixing between

694 magmatic and atmospheric gas within the volcano, and interaction between gas and meltwater causing

695 fractionation of elemental gas and carbon and nitrogen isotope ratios. It is likely that melting within void

696 spaces extends from FIC scales to much smaller soil pore scales, with widespread basal melting wherever heat

697 is sufficient. We cannot rule out the possibility that hydrothermal water could be sourced from a larger region

698 extending beneath Erebus' glaciated lower flanks. The presence of a hydrothermal system suggests that

699 previous phreatomagmatic activity may not be solely due to snow cover as previously assumed. Such a system

700 has the potential to dissolve a small proportion of the CO_2 that would otherwise be degassing. While the

701 carbon isotope ratios we measure can be attributed to dissolution of CO_2, the proportions of CO_2 we

702 measured would require a much higher proportion be dissolved. The small difference in CO_2 flux at sites

703 expected to be affected or unaffected by hydrothermal dissolution (about 2 $t \cdot d^{-1}$ between ITR and Tramway)

704 and the composition of the measured gases indicates that dilution by air is more likely to be responsible for

705 the relatively low proportion of CO_2 (< 3%).

706
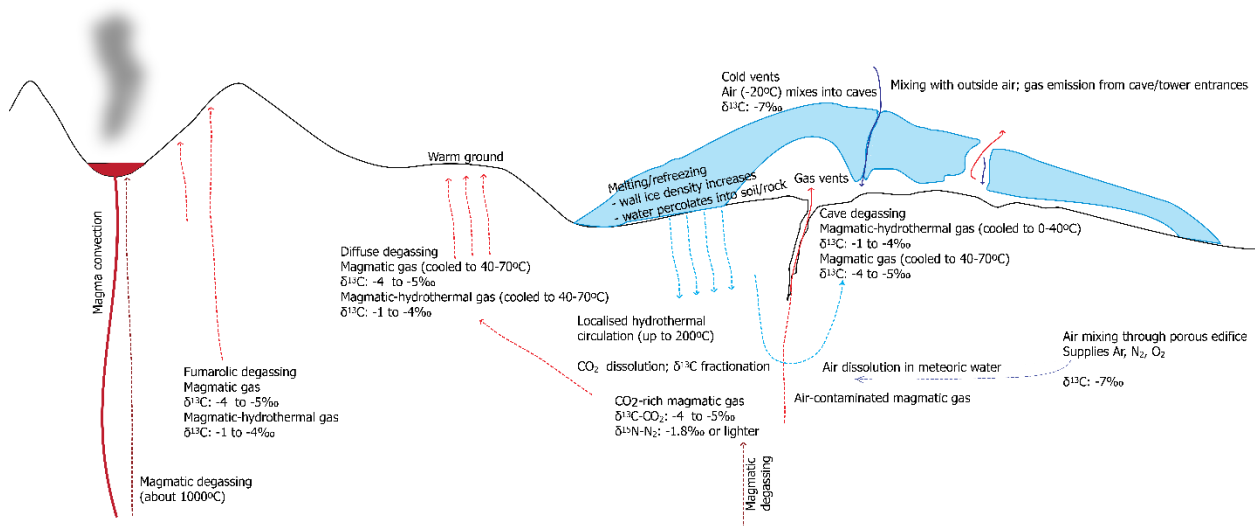
707
708 *Figure 12. Schematic of upper flank degassing on Erebus. The original magmatic signature is modified by air contamination,*
709 *and in some cases by interaction with a shallow hydrothermal system.*

710

711 While degassing from the Erebus summit crater has a partially shallow degassing signature affected by

712 processes occurring within or just below the lake (Oppenheimer et al., 2009; Iacovino, 2015; Ilanko et al.,

713 2015), upper flank degassing should be unaffected by conduit magma flow. Thus, gas measurements taken

714 over time at warm ground or FIC may give some indication as to changes occurring within the shallow

715 magma storage region, or to deeper sources of degassing. Our measurements show variations in small volume

716 copper tube samples that may be due to temporal changes over short time scales. High resolution time series

717 measurements in the field, of both composition and carbon isotope ratios, could be advantageous to

718 understand high frequency variations. Field gas analyses for carbon isotope ratios are possible (Di Martino et

719 al., 2016), but the power requirements and stable conditions currently required for analyses in the field pose a

720 particular challenge on Erebus.

721
722
5. Conclusions
724

725   Despite contributing a relatively small proportion of the gas emitted from Erebus, low temperature degassing
726   sites reveal information about the shallow interactions between magmatic gas, meltwater, and atmospheric air
727   in the shallow volcanic edifice. The loss of CO_2 to the hydrothermal system has been estimated and its effects
728   are seen in carbon isotope ratios of CO_2. Magmatic values are around -4‰, with fractionation to heavier
729   values related to dissolution in water. Melting is observed in the warm cave environments and may contribute
730   meteoric water to hydrothermal systems. Water availability varies locally, with potential shallow systems
731   represented by high velocity structures such as that beneath Ice Tower Ridge (Zandomeneghi et al., 2013).
732   While the pre-existing dyke intrusion provides pathways for magmatic gas ascent, there is also a greater
733   degree of interaction with water at high temperatures, resulting in lower fluxes of CO_2, of about two-thirds of
734   that at Tramway Ridge, and fractionation towards heavier carbon isotope ratios closer to -1‰, as the carbon
735   isotopes equilibrate between gaseous CO_2 and other aqueous or precipitating phases, especially HCO_3^-, and
736   possibly calcite. By contrast, shallow magma bodies at Sauna and Tramway suggested by low seismic velocity
737   regions (Zandomeneghi et al., 2013) are associated with higher CO_2 fluxes and carbon isotope ratios less
738   affected by shallow water or air interaction.
739

740   Samples at many sites contain a high proportion of air, showing that in addition to removal by dissolution,
741   initial concentrations of CO_2 are diluted by air. Although this dilution may be shallow and localized, oxygen
742   depleted samples also contain air-derived nitrogen, indicating that further modification causing oxygen
743   removal must have occurred after air contamination. This suggests that atmospheric air mixes with the
744   magmatic gas more systematically, possibly from wind-driven mountain breathing through the volcanic
745   edifice. Nitrogen isotope ratios show that most samples are heavily influenced by air contamination. Oxygen-
746   poor samples could then result from the removal of air-derived oxygen, though the exact mechanism, for
747   example redox reactions with rocks, or microbial processes, remains unknown.
748

749   The identification and characterization of a liquid-dominated hydrothermal system at Erebus has important
750   implications for availability of liquid water in the subsurface, and the potential for phreatomagmatic
751   eruptions. A warm liquid water phase also provides an additional and previously unrecognized habitat for
752   microorganisms living below the ice and permafrost region of the volcanic edifice.
753
754

760

References

762 ASPA No. 175 management plan, 2014. Management Plan for Antarctic Specially Protected Area No.
763   175. High Altitude Geothermal Sites of the Ross Sea Region (including parts of the summits of
764   Mount Erebus, Ross Island and Mount Melbourne and Mount Rittmann, northern Victoria Land),

765   in: ATCM XXXVII Final Report. Presented at the Antarctic Treaty Consultative Meeting,
766   Brasilia, pp. 199-225. https://www.ats.aq/documents/recatt/att553_e.pdf.
767 Assonov, S.S., Brenninkmeijer, C.A.M., Jöckel, P., 2005. The 18O isotope exchange rate between firn air
768   CO2 and the firn matrix at three Antarctic sites. J. Geophys. Res. Atmospheres 110, D18310.
769   https://doi.org/10.1029/2005JD005769
770 Barfod, D.N., Ballentine, C.J., Halliday, A.N., Fitton, J.G., 1999. Noble gases in the Cameroon line and
771   the He, Ne, and Ar isotopic compositions of high μ (HIMU) mantle. J. Geophys. Res. Solid Earth
772   104, 29509–29527. https://doi.org/10.1029/1999JB900280
773 Barry, P.H., Hilton, D.R., Füri, E., Halldórsson, S.A., Grönvold, K., 2014. Carbon isotope and abundance
774   systematics of Icelandic geothermal gases, fluids and subglacial basalts with implications for
775   mantle plume-related CO_2 fluxes. Geochim. Cosmochim. Acta 134, 74–99.
776   https://doi.org/10.1016/j.gca.2014.02.038
777 Behrendt, J.C., 1999. Crustal and lithospheric structure of the West Antarctic Rift System from
778   geophysical investigations - a review. Glob. Planet. Change 23, 25–44.
779   https://doi.org/10.1016/S0921-8181(99)00049-1
780 Behrendt, J.C., LeMasurier, W.E., Cooper, A.K., Tessensohn, F., Tréhu, A., Damaske, D., 1991.
781   Geophysical studies of the West Antarctic Rift System. Tectonics 10, 1257–1273.
782   https://doi.org/10.1029/91TC00868
783 Bergfeld, D., Evans, W.C., Howle, J.F., Hunt, A.G., 2015. Magmatic gas emissions at Holocene volcanic
784   features near Mono Lake, California, and their relation ot regional magmatism. J. Volcanol.
785   Geotherm. Res. 292, 70–83.
786 Bottinga, Y., 1968. Calculated fractionation factors for carbon and hydrogen isotope exchange in the
787   system carbon dioxide-graphite-methane-hydrogen-water vapor. Geochim. Cosmochim. Acta 33,
788   49–64.
789 Bräuer, K., Geissler, W.H., Kämpf, H., Niedermannn, S., Rman, N., 2016. Helium and carbon isotope
790   signatures of gas exhalations in the westernmost part of the Pannonian Basin (SE Austria/NE
791   Slovenia): Evidence for active lithospheric mantle degassing. Chem. Geol. 422, 60–70.
792   https://doi.org/10.1016/j.chemgeo.2015.12.016
793 Camarda, M., De Gregorio, S., Favara, R., Gurrieri, S., 2007. Evaluation of carbon isotope fractionation
794   of soil CO_2 under an advective–diffusive regimen: A tool for computing the isotopic composition
795   of unfractionated deep source. Geochim. Cosmochim. Acta 71, 3016–3027.
796   https://doi.org/10.1016/j.gca.2007.04.002
797 Cartigny, P., 2005. Stable Isotopes and the Origin of Diamond. Elements 1, 79–84.
798   https://doi.org/10.2113/gselements.1.2.79
799 Cartigny, P., Jendrzejewski, N., Pineau, F., Petit, E., Javoy, M., 2001. Volatile (C, N, Ar) variability in
800   MORB and the respective roles of mantle source heterogeneity and degassing: the gase of the
801   Southwest Indian Ridge. Earth Planet. Sci. Lett. 194, 241–257.
802 Chiodini, G., Allard, P., Caliro, S., Parello, F., 2000. 18O exchange between steam and carbon dioxide in
803   volcanic and hydrothermal gases: implications for the source of water. Geochim. Cosmochim.
804   Acta 64, 2479–2488. https://doi.org/10.1016/S0016-7037(99)00445-7
805 Chiodini, G., Cioni, R., Guidi, M., Raco, B., Marini, L., 1998. Soil CO_2 flux measurements in volcanic
806   and geothermal areas. Appl. Geochem. 13, 543–552. https://doi.org/10.1016/S0883-
807   2927(97)00076-0
808 Christoffersen, P., Bougamont, M., Carter, S.P., Fricker, H.A., Tulaczyk, S., 2014. Significant
809   groundwater contribution to Antarctic ice streams hydrologic budget. Geophys. Res. Lett. 41,
810   2003–2010. https://doi.org/10.1002/2014GL059250
811 Cigna, A.A., 1968. An analytical study of air circulation in caves. Int. J. Speleol. 3, 41–54.
812   https://doi.org/10.5038/1827-806X.3.1.3
813 Clark, I.D., Fritz, P., 1997. Environmental Isotopes in Hydrogeology. CRC Press, Boca Raton, FL.
814 Correale, A., Paonita, A., Rizzo, A.L., Grassa, F., Martelli, M., 2015. The carbon-isotope signature of
815   ultramafic xenoliths from the Hyblean Plateau (southeast Sicily, Italy): Evidence of mantle

heterogeneity. Geochem. Geophys. Geosystems 16, 600–611.
https://doi.org/10.1002/2014GC005656

Correale, A., Pelorosso, B., Rizzo, A.L., Coltorti, M., Italiano, F., Bonadiman, C., 2017. A geochemical
study of lithospheric mantle beneath Northern Victoria Land (Antarctica): main evidences from
volatile content in ultramafic xenoliths, in: Geophysical Research Abstracts. Presented at the
EGU General Assembly, European Geosciences Union, Vienna, pp. EGU2017-17484.

Curtis, A., 2015. Dynamics and global relevance of fumarolic ice caves on Erebus Volcano, Antarctica
(Ph.D). New Mexico Institute of Mining and Technology, Socorro.

Curtis, A., Kyle, P.R., 2017. Methods for mapping and monitoring global glaciovolcanism. J. Volcanol.
Geotherm. Res. 333–334, 134–144. https://doi.org/10.1016/j.jvolgeores.2017.01.017

Curtis, A., Kyle, P.R., 2011. Geothermal point sources identified in a fumarolic ice cave on Erebus
volcano, Antarctica using fiber optic distributed temperature sensing. Geophys. Res. Lett. 38.
https://doi.org/10.1029/2011GL0482

Curtis, A., Kyle, P.R., 2010. Erebus caves database. https://doi.org/10.15784/600381

D'Alessandro, W., Giammanco, S., Parello, F., 1997. CO_2 output and d13C(CO_2) from Mount Etna as
indicators of degassing of shallow asthenosphere. Bull. Volcanol. 58, 455–458.

de Moor, J.M., Fischer, T.P., Sharp, Z.D., Hilton, D.R., Barry, P.H., Mangasini, F., Ramirez, C., 2013.
Gas chemistry and nitrogen isotope compositions of cold mantle gases from Rungwe Volcanic
Province, southern Tanzania. Chem. Geol., Frontiers in Gas Geochemistry 339, 30–42.
https://doi.org/10.1016/j.chemgeo.2012.08.004

Di Martino, M.R., Capasso, G., Camarda, M., 2016. Spatial domain analysis of carbon dioxide from soils
on Vulcano Island: implications for CO_2 ouput evaluation. Chem. Geol. 444, 59–70.
https://doi.org/10.1016/j.chemgeo.2016.09.037

Dibble, R.R., Kyle, P.R., Skov, M.J., 1994. Volcanic activity and seismicity of Mount Erebus, 1986-1994.
Antarct. J. U. S. 29, 11–14.

Faimon, J., Troppova, D., Baldik, V., Novotny, R., 2012. Air circulation and its impact on microclimatic
variables in the Cısarska Cave (Moravian Karst, Czech Republic). Int. J. Climatol. 32, 599–623.
https://doi.org/10.1002/joc.2298

Federico, C., Corso, P.P., Fiordilino, E., Cardellini, C., Chiodini, G., Parello, F., Pisciotta, A., 2010.
CO_2 degassing at La Solfatara volcano (Phlegrean Fields): Processes affecting $\delta^{13}C$ and $\delta^{18}O$ of
soil CO_2. Geochim. Cosmochim. Acta 74, 3521–3538. https://doi.org/10.1016/j.gca.2010.03.010

Fielding, C.R., Browne, G.H., Field, B., Florindo, F., Harwood, D.M., Krissek, L.A., Levy, R.H., Panter,
K.S., Passchier, S., Pekar, S.F., 2011. Sequence stratigraphy of the ANDRILL AND-2A drillcore,
Antarctica: A long-term, ice-proximal record of Early to Mid-Miocene climate, sea-level and
glacial dynamism. Palaeogeogr. Palaeoclimatol. Palaeoecol. 305, 337–351.
https://doi.org/10.1016/j.palaeo.2011.03.026

Fischer, Takahata, N., Sano, Y., Sumino, H., Hilton, D.R., 2005. Nitrogen isotopes of the mantle: insights
from mineral separates. Geophys. Res. Lett. 32, L11305. https://doi.org/10.1029/2005GL022792

Fischer, T.P., Chiodini, G., 2015. Volcanic, Magmatic and Hydrothermal Gases, in: Sigurdsson, H.,
Houghton, B., McNutt, S., Rymer, H., Stix, J. (Eds.), The Encyclopedia of Volcanoes. pp. 779–
797.

Fischer, T.P., Lopez, T.M., 2016. First airborne samples of a volcanic plume for $\delta^{13}C$ of CO_2
determinations. Geophys. Res. Lett. 43, 2016GL068499. https://doi.org/10.1002/2016GL068499

Flowers, G.E., 2015. Modelling water flow under glaciers and ice sheets. Proc. R. Soc. Math. Phys. Eng.
Sci. 471, 20140907–20140907. https://doi.org/10.1098/rspa.2014.0907

Gerlach, T.M., Taylor, B.E., 1990. Carbon isotope constraints on degassing of carbon dioxide from
Kilauea Volcano. Geochim. Cosmochim. Acta 54, 2051–2058. https://doi.org/10.1016/0016-
7037(90)90270-U

Giggenbach, W.F., 1987. Redox processes governing the chemistry of fumarolic gas discharges from
White Island. Appl. Geochem. 2, 143–161.

866 Giggenbach, W.F., 1975. A simple method for the collection and analysis of volcanic gas samples. Bull.
867   Volcanol. 39, 132–145. https://doi.org/10.1007/BF02596953
868 Hall, J., Wilson, T., Henrys, S., 2007. Structure of the central Terror Rift, western Ross Sea, Antarctica.
869   AK Cooper CR Raymond Al Eds Antarct. Keyst. Chang. World - Online Proc. 10th ISAES,
870   USGS Open-File Report 2007-1047 5. https://doi.org/10.3133/of2007-1047.srp108
871 Harpel, C.J., Kyle, P.R., Dunbar, N.W., 2008. Englacial tephrostratigraphy of Erebus volcano, Antarctica.
872   J. Volcanol. Geotherm. Res. 177, 549–568. https://doi.org/10.1016/j.jvolgeores.2008.06.001
873 Harry, D.L., Anoka, J.L., Jha, S., 2018. Geodynamic models of the West Antarctic Rift System:
874   Implications for the mantle thermal state. Geosphere 14, 2407–2429.
875   https://doi.org/10.1130/GES01594.1
876 Henrys, S., Wilson, T., Whittaker, J.M., Fielding, C., Hall, J., Naish, T., 2007. Tectonic history of mid-
877   Miocene to present southern Victoria Land Basin, inferred from seismic stratigraphy in McMurdo
878   Sound, Antarctica. AK Cooper CR Raymond Al Eds Antarct. Keyst. Chang. World - Online Proc.
879   10th ISAES, Open-File Report USGS Open-Fie Report 2007-1047, 4.
880   https://doi.org/10.3133/of2007-1047.srp049
881 Huybers, P., Langmuir, C., 2009. Feedback between deglaciation, volcanism, and atmospheric CO_2. Earth
882   Planet. Sci. Lett. 286, 479–491. https://doi.org/10.1016/j.epsl.2009.07.014
883 Iacovino, K., 2015. Linking subsurface to surface degassing at active volcanoes: A thermodynamic model
884   with applications to Erebus volcano. Earth Planet. Sci. Lett. 431, 59–74.
885   https://doi.org/10.1016/j.epsl.2015.09.016
886 Ilanko, T., Oppenheimer, C., Burgisser, A., Kyle, P.R., 2015. Cyclic degassing of Erebus volcano,
887   Antarctica. Bull. Volcanol. 77. https://doi.org/10.1007/s00445-015-0941-z
888 Iverson, N.A., Kyle, P.R., Dunbar, N.W., McIntosh, W.C., Pearce, N.J.G., 2014. Eruptive history and
889   magmatic stability of Erebus volcano, Antarctica: insights from englacial tephra. Geochem.
890   Geophys. Geosystems 15, 4180–4202. https://doi.org/10.1002/2014GC005435
891 Iverson, N.A., Lieb-Lappen, R., Dunbar, N.W., Obbard, R., Kim, E., Golden, E., 2017. The first physical
892   evidence of subglacial volcanism under the West Antarctic Ice Sheet. Sci. Rep. 7, 11457.
893   https://doi.org/10.1038/s41598-017-11515-3
894 Javoy, M., Pineau, F., Delorme, H., 1986. Carbon and nitrogen isotopes in the mantle. Chem. Geol.,
895   Isotopes in Geology—Picciotto Volume 57, 41–62. https://doi.org/10.1016/0009-2541(86)90093-
896   8
897 Javoy, M., Pineau, F., Iiyama, I., 1978. Experimental determination of the isotopic fractionation between
898   gaseous CO_2 and carbon dissolved in tholeiitic magma. Contrib. Mineral. Petrol. 67, 35–39.
899 Kyle, P.R., Moore, J.A., Thirwall, M.F., 1992. Petrologic Evolution of Anorthoclase Phonolite Lavas at
900   Mount Erebus, Ross Island, Antarctica. J. Petrol. 33, 849–875.
901   https://doi.org/10.1093/petrology/33.4.849
902 Lee, H., Fischer, T.P., de Moor, J.M., Sharp, Z.D., Takahata, N., Sano, Y., 2017. Nitrogen recycling at the
903   Costa Rican subduction zone: The role of incoming plate structure. Sci. Rep. 7, 13933.
904   https://doi.org/10.1038/s41598-017-14287-y
905 Lee, H., Muirhead, J.D., Fischer, T.P., Ebinger, C.J., Kattenhorn, S.A., Sharp, Z.D., Kianji, G., 2016.
906   Massive and prolonged deep carbon emissions associated with continental rifting. Nat. Geosci. 9,
907   145–149. https://doi.org/10.1038/ngeo2622
908 Lee, H., Sharp, Z.D., Fischer, Tobias P., 2015. Kinetic nitrogen isotope fractionation between air and
909   dissolved N_2 in water: Implications for hydrothermal systems. Geochem. J. 49, 571–573.
910   https://doi.org/10.2343/geochemj.2.0380
911 LeMasurier, W.E., 2008. Neogene extension and basin deepening in the West Antarctic rift inferred from
912   comparisons with the East African rift and other analogs. Geology 36, 247–250.
913   https://doi.org/10.1130/G24363A.1
914 LeMasurier, W.E., 1990. Late Cenozoic volcanism on the Antarctic Plate: An overview, in: LeMasurier,
915   W.E., Thomson, J.W., Baker, P.E., Kyle, P.R., Rowley, P.D., Smellie, J.L., Verwoerd, W.J.

(Eds.), Antarctic Research Series. American Geophysical Union, Washington, D. C., pp. 1–17. https://doi.org/10.1029/AR048p0001

Lewicki, J.L., Hilley, G.E., Tosha, T., Aoyagi, R., Yamamoto, K., Benson, S.M., 2007. Dynamic coupling of volcanic CO_2 flow and wind at the Horseshoe Lake tree kill, Mammoth Mountain, California. Geophys. Res. Lett. 34. https://doi.org/10.1029/2006GL028848

Li, Z., Hoflund, G.B., 2003. A review on complete oxidation of methane at low temperatures. J. Nat. Gas Chem. 12, 154–160.

Lough, A.C., Wiens, D.A., Barcheck, C.G., Anandakrishnan, S., Aster, R.C., Blankenship, D.D., Huerta, A.D., Nyblade, A., Young, D.A., Wilson, T.J., 2013. Seismic detection of an active subglacial magmatic complex in Marie Byrd Land, Antarctica. Nat. Geosci. 6, 1031–1035. https://doi.org/doi:10.1038/ngeo1992

Lowenstern, J.B., 2001. Carbon dioxide in magmas and implications for hydrothermal systems. Miner. Deposita 36, 490–502. https://doi.org/10.1007/s001260100185

Lyon, G.L., Giggenbach, W.F., 1974. Geothermal activity in Victoria Land, Antarctica. N. Z. J. Geol. Geophys. 17, 511–521. https://doi.org/10.1080/00288306.1973.10421578

Malinin, S.D., Kropotova, O.I., Grinenko, V.A., Vernadskiy, V.I., 1967. Experimental determination of equilibrium constants for carbon isotope exchange in the system CO_2 (g)-HCO_3 (sol) under hydrothermal conditions. Geochem. Int. 4, 764–771.

Martin, A.P., Cooper, A.F., Price, R.C., 2014. Increased mantle heat flow with on-going rifting of the West Antarctic rift system inferred from characterisation of plagioclase peridotite in the shallow Antarctic mantle. Lithos 190–191, 173–190. https://doi.org/10.1016/j.lithos.2013.12.012

Martin, R.S., Mather, T.A., Pyle, D.M., 2006. High-temperature mixtures of magmatic and atmospheric gases. Geochem. Geophys. Geosystems 7. https://doi.org/10.1029/2005GC001186

Marty, B., Zimmermann, L., 1999. Volatiles (He, C, N, Ar) in mid-ocean ridge basalts: Assesment of shallow-level fractionation and characterization of source composition. Geochim. Cosmochim. Acta 63, 3619–3633.

Mattey, D.P., 1991. Carbon dioxide solubility and carbon isotope fractionation in basaltic melt. Geochim. Cosmochim. Acta 55, 3467–3473. https://doi.org/10.1016/0016-7037(91)90508-3

Mikucki, J.A., Auken, E., Tulaczyk, S., Virginia, R.A., Schamper, C., Sorenson, K.I., Doran, P.T., Dugan, H., Foley, N., 2015. Deep groundwater and potential subsurface habitats beneath an Antarctic dry valley. Nat. Commun. 6, 6831. https://doi.org/10.1038/ncomms7831

Mohapatra, R.K., Murty, S.V.S., 2004. Nitrogen isotopic composition of the MORB mantle: A reevaluation. Geochem. Geophys. Geosystems 5, Q01001. https://doi.org/10.1029/2003GC000612

Mook, W.G., Bommerson, J.C., Staverman, W.H., 1974. Carbon isotope fractionation between dissolved bicarbonate and gaseous carbon dioxide. Earth Planet. Sci. Lett. 22, 169–176. https://doi.org/10.1016/0012-821X(74)90078-8

Myrttinen, A., Becker, V., Barth, J.A.C., 2012. A review of methods used for equilibrium isotope fractionation investigations between dissolved inorganic carbon and CO_2. Earth-Sci. Rev. 115, 192–199. https://doi.org/10.1016/j.earscirev.2012.08.004

Ogretim, E., Crandall, D., Gray, D.D., Bromhal, G.S., 2013. Effects of atmospheric dynamics on CO_2 seepage at Mammoth Mountain, California, USA. J. Comput. Multiph. Flows 5, 283–294.

Oppenheimer, C., Kyle, P.R., 2008. Probing the magma plumbing of Erebus volcano, Antarctica, by open-path FTIR spectroscopy of gas emissions. J. Volcanol. Geotherm. Res. 177, 743–754. https://doi.org/10.1016/j.jvolgeores.2007.08.022

Oppenheimer, C., Lomakina, A.S., Kyle, P.R., Kingsbury, N.G., Boichu, M., 2009. Pulsatory magma supply to a phonolite lava lake. Earth Planet. Sci. Lett. 284, 392–398. https://doi.org/10.1016/j.epsl.2009.04.043

965 Oppenheimer, C., Moretti, R., Kyle, P.R., Eschenbacher, A., Lowenstern, J.B., Hervig, R.L., Dunbar,
966   N.W., 2011. Mantle to surface degassing of alkalic magmas at Erebus volcano, Antarctica. Earth
967   Planet. Sci. Lett. 306, 261–271. https://doi.org/10.1016/j.epsl.2011.04.005
968 Panter, K.S., Castillo, P., Krans, S., Deering, C., McIntosh, W., Valley, J.W., Kitajima, K., Kyle, P., Hart,
969   S., Blusztajn, J., 2018. Melt Origin across a Rifted Continental Margin: a Case for Subduction-
970   related Metasomatic Agents in the Lithospheric Source of Alkaline Basalt, NW Ross Sea,
971   Antarctica. J. Petrol. 59, 517–558. https://doi.org/10.1093/petrology/egy036
972 Panter, K.S., Winter, B., 2008. Geology of the Side Crater of the Erebus volcano, Antarctica. J. Volcanol.
973   Geotherm. Res., Volcanology of Erebus volcano, Antarctica 177, 578–588.
974 Phillips, E.H., Sims, K.W.W., Blichert-Toft, J., Aster, R.C., Gaetani, G.A., Kyle, P.R., Wallace, P.J.,
975   Rasmussen, D.J., 2018. The nature and evolution of mantle upwelling at Ross Island, Antarctica,
976   with implications for the source of HIMU lavas. Earth Planet. Sci. Lett. 498, 38–53.
977   https://doi.org/10.1016/j.epsl.2018.05.049
978 Rasmussen, D.J., Kyle, P.R., Wallace, P.J., Sims, K.W.W., Gaetani, G.A., Phillips, E.H., 2017.
979   Understanding Degassing and Transport of CO_2-rich Alkalic Magmas at Ross Island, Antarctica
980   using Olivine-Hosted Melt Inclusions. J. Petrol. 58, 841–861.
981   https://doi.org/10.1093/petrology/egx036
982 Resing, J.A., Lupton, J.E., Feely, R.A., Lilley, M.D., 2004. CO_2 and ^{3}He in hydrothermal plumes:
983   implications for mid-ocean ridge CO_2 flux. Earth Planet. Sci. Lett. 226, 449–464.
984   https://doi.org/10.1016/j.epsl.2004.07.028
985 Rilling, S., Mukasa, S., Wilson, T., Lawver, L., Hall, C., 2009. New determinations of 40Ar/39Ar
986   isotopic ages and flow volumes for Cenozoic volcanism in the Terror Rift, Ross Sea, Antarctica -
987   Rilling - 2009 - Journal of Geophysical Research: Solid Earth - Wiley Online Library. J.
988   Geophys. Res. 114. https://doi.org/10.1029/2009JB006303
989 Rocchi, S., Armienti, P., D'Orazio, M., Tonarini, S., Wijbrans, J.R., Vincenzo, G.D., 2002. Cenozoic
990   magmatism in the western Ross Embayment: Role of mantle plume versus plate dynamics in the
991   development of the West Antarctic Rift System. J. Geophys. Res. Solid Earth 107, ECV 5-1-ECV
992   5-22. https://doi.org/10.1029/2001JB000515
993 Rothman, L.S., Gordon, I.E., Babikov, Y., Barbe, A., Chris Benner, D., Bernath, P.F., Birk, M.,
994   Bizzocchi, L., Boudon, V., Brown, L.R., Campargue, A., Chance, K., Cohen, E.A., Coudert,
995   L.H., Devi, V.M., Drouin, B.J., Fayt, A., Flaud, J.-M., Gamache, R.R., Harrison, J.J., Hartmann,
996   J.M., Hill, C., Hodges, J.T., Jacquemart, D., Jolly, A., Lamouroux, J., Le Roy, R.J., Li, G., Long,
997   D.A., Lyulin, O.M., Mackie, C.J., Massie, S.T., Mikhailenko, S.N., Müller, H.S.P., Naumenko,
998   O.V., Nikitin, A.V., Orphal, J., Perevalov, V.I., Perrin, A., Polovtseva, E.R., Richard, C., Smith,
999   M.A.H., Starikova, E., Sung, K., Tashkun, S.A., Tennyson, J., Toon, G.C., Tyuterev, V.G.,
1000   Wagner, G., 2013. The HITRAN2012 molecular spectroscopic database. J. Quant. Spectrosc.
1001   Radiat. Transf. 130, 4–50.
1002 Sander, R., 2015. Compilation of Henry's law constants (version 4.0) for water as solvent. Atmospheric
1003   Chem. Phys. 15, 4399–4981. https://doi.org/10.5194/acp-15-4399-2015
1004 Sano, Y., Takahata, N., Nishio, Y., Fischer, T.P., Williams, S.N., 2001. Volcanic flux of nitrogen from
1005   the Earth. Chem. Geol. 171, 263–271. https://doi.org/10.1016/S0009-2541(00)00252-7
1006 Sano, Y., Tokutake, T., Takahata, N., 2008. Accurate Measurement of Atmospheric Helium Isotopes.
1007   Anal. Sci. 24, 521–525. https://doi.org/10.2116/analsci.24.521
1008 Scopelliti, G., Bellanca, A., Neri, R., 2011. Petrography and carbonate isotope stratigraphy from MIS
1009   AND-1B core, Antarctica: Evidence of the early Pliocene warming event. Glob. Planet. Change
1010   76, 22–32. https://doi.org/10.1016/j.gloplacha.2010.11.006
1011 Sims, K.W.W., Blichert-Toft, J., Kyle, P.R., Pichat, S., Gauthier, P.-J., Blusztajn, J., Kelly, P., Ball, L.,
1012   Layne, G., 2008. A Sr, Nd, Hf, and Pb isotope perspective on the genesis and long-term evolution
1013   of alkaline magmas from Erebus volcano, Antarctica. J. Volcanol. Geotherm. Res. 177, 606–618.
1014   https://doi.org/doi: DOI: 10.1016/j.jvolgeores.2007.08.006

1015 Symonds, R.B., Gerlach, T.M., Reed, M.H., 2001. Magmatic gas scrubbing: implications for volcano
1016   monitoring. J. Volcanol. Geotherm. Res. 108, 303–341. https://doi.org/10.1016/S0377-
1017   0273(00)00292-4
1018 Szaran, J., 1997. Achievement of carbon isotope equilibrium in the system HCO^{3-} (solution) - CO^{2} (gas).
1019   Chem. Geol. 142, 79–86. https://doi.org/10.1016/S0009-2541(97)00077-6
1020 Tebo, B.M., Davis, R.E., Anitori, R.P., Connell, L.B., Schiffman, P., Staudigel, H., 2015. Microbial
1021   communities in dark oligotrophic volcanic ice cave ecosystems of Mt. Erebus, Antarctica. Front.
1022   Microbiol. 6. https://doi.org/10.3389/fmicb.2015.00179
1023 Thorstenson, D.C., Weeks, E.P., Haas, H., Busenberg, E., Plummer, L.N., Peters, C.A., 1998. Chemistry
1024   of unsaturated zone gases sampled in open boreholes at the crest of Yucca Mountain, Nevada:
1025   Data and basic concepts of chemical and physical processes in the mountain. Water Resour. Res.
1026   34, 1507–1529. https://doi.org/10.1029/98WR00267
1027 van Wyk de Vries, M., Bingham, R.G., Hein, A.S., 2018. A new volcanic province: an inventory of
1028   subglacial volcanoes in West Antarctica. Geol. Soc. Lond. Spec. Publ. 461, 231–248.
1029   https://doi.org/10.1144/SP461.7
1030 Wardell, L.J., Kyle, P.R., Campbell, A.R., 2003. Carbon dioxide emissions from fumarolic ice towers,
1031   Mount Erebus volcano, Antarctica, in: Volcanic Degassing, Special Publication. Geological
1032   Society, London, pp. 231–246.
1033 Woodcock, A.H., 1987. Mountain breathing revisited - the hyperventilation of a volcano cinder cone.
1034   Bull. Am. Meteorol. Soc. 68, 125–130. https://doi.org/10.1175/1520-
1035   0477(1987)068<0125:MBRHOA>2.0.CO;2
1036 Zandomeneghi, D., Aster, R., Kyle, P.R., Barclay, A., Chaput, J., Knox, H., 2013. Internal structure of
1037   Erebus volcano, Antarctica imaged by high-resolution active-source seismic tomography and
1038   coda interferometry. J. Geophys. Res. Solid Earth 118, 1067–1078.
1039   https://doi.org/10.1002/jgrb.50073
1040 Zhang, J., Quay, P.D., Wilbur, D.O., 1995. Carbon isotope fractionation during gas-water exchange and
1041   dissolution of CO2. Geochim. Cosmochim. Acta 59, 107–114.
1042 Zimbelman, D.R., Rye, R.O., Landis, G.P., 2000. Fumaroles in ice caves on the summit of Mount
1043   Rainier: preliminar stable isotope, gas, and geochemical studies. J. Volcanol. Geotherm. Res. 97,
1044   457–473. https://doi.org/10.1016/S0377-0273(99)00180-8
1045
1046

1047   SM1: CO_2/O_2 ratios
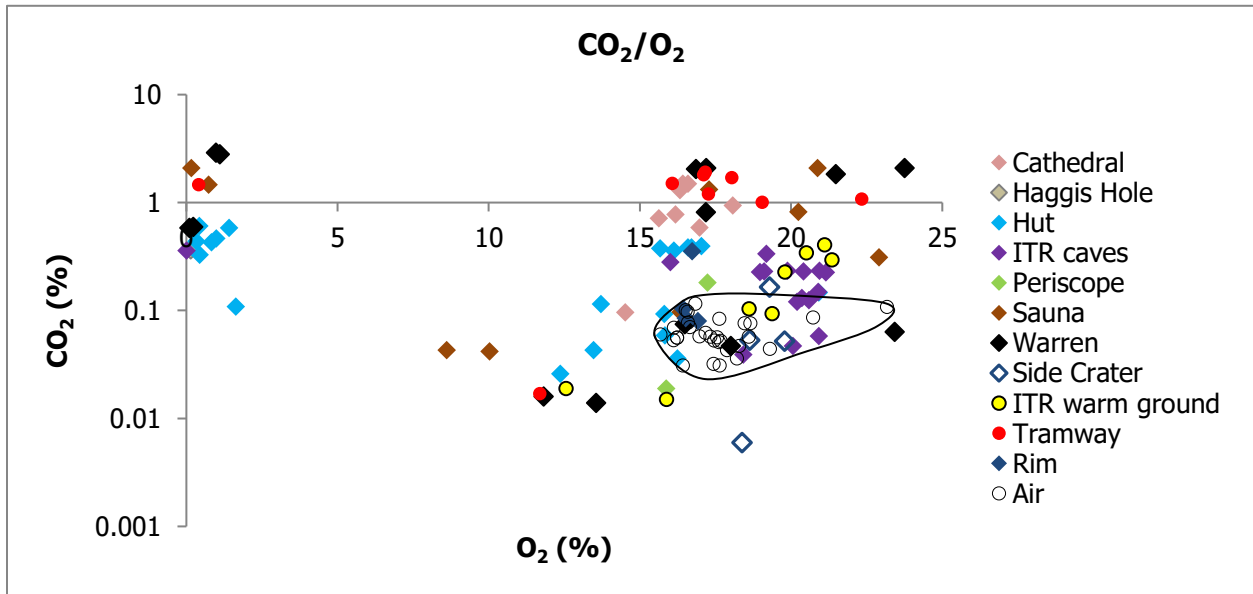
1048

1049 CO_2/O_2 from GC-QMS showing samples with air-like or higher CO_2 can be oxygen depleted. Samples
1050   with intermediate oxygen levels between air and oxygen depleted samples have CO_2 content of 140 -
1051   1100 ppm (the most CO_2 depleted sample is from a Giggenbach bottle in 2015 that has airlike O_2 but
1052   about 60 ppm CO_2).

1053   SM2: Table of samples analysed by GC-QMS with approximate latitude & longitude